# Autophagy regulator ATG7 links energy metabolism to tubular cell fate specialization and kidney disease

Daniela Nieri[1*], Svenja Aline Keller[1*], Zhiyong Chen[1], Roberto Pili[2], Adia M. Ouellette[3,4], Marine Berquez[1], Patrick Krohn[1], Federica Carloni[1], Andrea Raimondi[5,6], Valeria Berno[6], Martina Zanella[7], Michelle Elisabeth Reid[7], Alaa Othman[7], Andrew M. Schaefer[8,9], Eric Gregory Olinger[10,11], John A. Sayer[11,12,13], Alina Ustiugova[14], Mikhail Korzinkin[14], Stephan C.F. Neuhauss[15], Christian Münz[16], Robert McFarland[8,9], Robert W. Taylor[8,9], Louis R. Lapierre[3,4], Elisa Araldi[2,17], Olivier Devuyst[1,#], and Alessandro Luciani[1,#]

[1] Institute of Physiology, University of Zurich, 8057 Zurich, Switzerland;
[2] Systems Medicine Laboratory, Department of Medicine and Surgery, University of Parma, 43125 Parma, Italy ;
[3] Department of Chemistry and Biochemistry, University of Moncton, NB E1A 3E9 Moncton, Canada;
[4] New Brunswick Center for Precision Medicine, 27 rue Providence, Moncton, NB E1C 8X3, Canada;
[5] Institute for Research in Biomedicine, Università della Svizzera Italiana (USI), CH-6500 Bellinzona, Switzerland;
[6] San Raffaele Scientific Institute, Experimental Imaging Center, 20132 Milan, Italy;
[7] Functional Genomics Center Zurich, University of Zurich, 8057, Zurich, Switzerland;
[8] Mitochondrial Research Group, Translational and Clinical Research Institute, Faculty of Medical Sciences, Newcastle University, Newcastle upon Tyne, NE2 4HH, UK
[9] NHS Highly Specialised Service for Rare Mitochondrial Disorders, Newcastle upon Tyne Hospitals NHS Foundation Trust, Newcastle upon Tyne, NE1 4LP, UK
[10] Center for Human Genetics Cliniques Universitaires Saint-Luc, UCLouvain, 1200 Brussels Belgium;
[11] Biosciences Institute, Faculty of Medical Sciences, Newcastle University, NE Newcastle upon Tyne, NE1 3BZ, UK;
[12] Renal Services, Newcastle Upon Tyne Hospitals NHS Foundation Trust, Newcastle upon Tyne, NE7 7DN, UK;
[13] NIHR Newcastle Biomedical Research Centre, Newcastle University, Newcastle upon Tyne, NE4 5PL, United Kingdom;
[14] Insilico Medicine Hong Kong Ltd., Hong Kong Science and Technology Park, Hong Kong, Hong Kong SAR, China;
[15] Department of Molecular Life Sciences, and [16] Institute of Experimental Immunology, University of Zurich, 8057 Zurich, Switzerland;

[17] Computational Biomedicine, University Medical Center of the Johannes Gutenberg University Mainz, 55131 Mainz, Germany

*Equal first authors; [#]Co-directed the study

Correspondence: alessandro.luciani@uzh.ch

**Abstract**

Precise coupling between differentiation and metabolism in the kidney proximal tubule (PT) is critical for homeostasis, yet determinants of tubular cell fate specialization remain unclear. Using genetically engineered model organisms, cell cultures, proteomic and metabolomic profiling, and human genetics, we show that ATG7 deficiency shifts PT cell metabolism and differentiation toward growth at the expense of function. ATG7 loss impairs autophagy-mediated lipid droplet homeostasis, causing their accumulation and disrupting fatty acid transfer to mitochondria, compromising energy metabolism and cellular function. In zebrafish, reintroducing human wild-type ATG7 restores homeostasis, whereas inhibiting mitochondrial fatty acid oxidation induces phenotypic changes in wild-type cells. In humans, *ATG7* variation associates with increased kidney disease risk, and loss-of-function variants cause tubular proteinuria and altered mitochondrial metabolism. Low *ATG7* levels correlate with dedifferentiation, altered metabolic pathways, and poor renal cell carcinoma outcomes. Together, our results establish a metabolic paradigm that links autophagy to kidney epithelial cell fate specialization, with broad implications for health and disease.

## Introduction

Epithelial cells have developed elaborate mechanisms to efficiently assimilate nutrients from their surroundings, a crucial process for maintaining homeostasis.[1,2] Any disruption in these processes can lead to dysfunction and disease. This is particularly evident in the kidney, where epithelial cells lining the proximal tubule (PT) utilise highly developed endocytosis and lysosome-related pathways to reabsorb and metabolise plasma proteins and solutes ultrafiltered from the bloodstream, preventing their loss in the urine.[3,4] Dysregulation of these pathways, whether from congenital or acquired conditions, steers the differentiation of PT cells towards anabolic programs for growth and proliferation, impairing their functioning state and resulting in abnormal excretion of vital nutrients in the urine — a typical marker of kidney damage.[3,4]

The reabsorption of ultrafiltered, low-molecular-weight (LMW) proteins by PT cells involves the multi-ligand receptors LRP2/megalin and cubilin and the CUBN-associated protein amnionless.[5] Upon internalization, these receptors and ligands dissociate within acidified endosomes. The receptors are recycled to the plasma membrane while the ligands are sorted into lysosomes for degradation.[6] Beyond endocytosis, lysosomes terminate macroautophagy/autophagy – an evolutionarily conserved pathway that safeguards homeostasis by breaking down macromolecules and organelles encapsulated in autophagosomes.[7] Alterations in autophagy levels, arising from lysosome dysfunction, have been implicated in PT dedifferentiation and proximal tubulopathy, further substantiating their critical role in homeostasis and kidney health.[8-11]

A set of evolutionarily conserved autophagy-related (ATG) gene products orchestrate the assembly and elongation of the autophagosome membrane.[12] This fundamental process operates continuously at low levels and is further induced under various stress conditions, involving the generation, scrambling, and transport of lipids.[13] Ubiquitin-like conjugation systems – ATG12 coupling to ATG5 for association with ATG16L1, and ATG8/MAP1LC3 binding to membrane-resident phosphatidylethanolamine – aid in autophagosome formation and maintenance of autophagy.[14,15] ATG7 – an autophagy protein with E1-like enzymatic

activity – activates ATG12 linkage to ATG5 and promotes MAP1LC3-I lipidation.[16] This process yields MAP1LC3-II – a bona fide biosensor for monitoring autophagy levels in cells and tissues.[17]

The disruption of endogenous ATG proteins has been crucial in revealing autophagy's contribution to tissue development and organ-wide physiology.[18] Mice with constitutive loss of ATG7 exhibit metabolic abnormalities and neonatal mortality.[19] Tissue-specific ATG7 deficiency substantiated the role of autophagy in connecting the cellular stress response to homeostasis. In the PT cells of murine kidneys, the absence of ATG7 hinders autophagy-driven mechanisms of cellular adaptation to stress, contributing to maladaptation and disease development.[20,21] Although ATG7-mediated autophagy has been extensively studied in the context of cellular stress response and adaptation, its baseline role in balancing the proliferation and differentiation of PT epithelial cells, and thus maintaining their specialized function, remains poorly understood.

The kidneys rank among the most energy-demanding organs, with PT cells featuring the highest densities of mitochondria.[22,23] These organelles enable the tubular cells to maintain their metabolic homeostasis and perform specialized functions.[24,25] Defects in mitochondria can disrupt energy metabolism, impairing PT differentiation and contributing to disease development.[10,11,26] Restoring healthy mitochondrial metabolic activities through interventions targeting autophagy has shown promise in mitigating kidney disease development in preclinical models.[27,28] Recent evidence of defective neurodevelopment in patients harbouring biallelic pathogenic *ATG7* variants further emphasizes the importance of autophagy in health and homeostasis.[29]

Here, we utilize model organisms and physiologically relevant cell culture systems and integrate them with protein and metabolite profiling, alongside population and patient studies, to characterize the causal role of ATG7-mediated autophagy as a determinant of cell fate specialization and differentiation of kidney tubule epithelium. Together the results reveal insights into the fundamental mechanisms of homeostasis and disease, providing potential therapeutic approaches for currently intractable disorders.

## Results

### *Atg7 deficiency impairs autophagy in the proximal tubule epithelial cells*

To investigate the consequences of autophagy deficiency on PT cells, we generated a mouse model with a targeted deletion of ATG7 by crossbreeding *Atg7*$^{fl/fl}$ mice[16] with a γ*Gt1*-cre mouse line[30] where gamma-glutamyl transferase 1 (γGt1) is specifically expressed in the PT segments (**Fig. 1a-b; Supplementary Fig. 1a-c**). The resulting conditional PT-specific *Atg7* knockout mice (*Atg7*$^{fl/fl}$ ; γ*Gt1*$^{cre/cre}$ hereafter referred to as *Atg7*$^{PT\text{-}KO}$) were viable at expected Mendelian frequencies, with maintained female-to-male ratios. Littermate mice (*Atg7*$^{fl/fl}$; γ*Gt1*$^{wt/wt}$ hereafter referred to as CTR) were used for comparison. The deletion of *Atg7* was confirmed by polymerase chain reaction (PCR) analysis of genomic DNA samples (**Supplementary Fig. 1d**) and validated in kidney cortex samples using real-time quantitative PCR (RT-qPCR) and immunoblotting analyses (**Fig. 1c-d**). *Atg7* transcript levels remained unchanged in the liver, heart, and intestine, confirming the specificity of the deletion (**Supplementary Fig. 1e**). Kidney tissue samples from *Atg7*$^{PT\text{-}KO}$ mice exhibited a significant decrease in the steady-state levels of the lipidated, autophagosome-associated form of Map1lc3b (Map1lc3b-II) compared to their control littermates (**Fig. 1e**). Additionally, an accumulation of Sequestosome 1 (Sqstm1), a selective degradation substrate of autophagy[7,12,13,17], was observed in the PT of mutant kidneys (**Fig. 1e-f**). Together, these results indicate that selective ATG7 deficiency hampers the basal levels of autophagy in the epithelial cells lining the PT of mouse kidneys.

### *Defective Atg7-driven autophagy triggers dyshomeostasis and PT dysfunction*

Next, we tested whether alterations in ATG7-driven autophagy disrupt the nutrient homeostasis and reabsorptive activities of PT cells. We followed a cohort of *Atg7*$^{PT\text{-}KO}$ mice and CTR littermates up to 24 weeks of age (**Fig. 2a; Supplementary Table 1**). From 12 weeks of age, we observed a decrease in body weight and growth delay in mutant mice compared to CTR littermates (**Fig. 2b,c**). We then monitored the appearance in the urine of plasma proteins and electrolytes to investigate whether loss of ATG7 and impaired

autophagy lead to PT dysfunction (renal Fanconi syndrome[3,4]). Urinary levels of Clara cell secretory protein 16 (CC16), a typical marker of PT dysfunction, were significantly increased in *Atg7*$^{PT\text{-}KO}$ compared to CTR mice as early as 4 weeks of age, irrespective of gender (**Fig. 2d; Supplementary Fig. 2a**). The abnormal appearance in the urine of plasma proteins including albumin, transferrin (TF) and vitamin D binding protein (VDBP) further confirmed the tubular defects in mutant mice (**Fig. 2e,f**). Other indicators of kidney PT dysfunction, such as glucosuria, phosphaturia, calciuria, and polyuria (**Fig. 2g,h; Supplementary Fig. 2b,c; Supplementary Table 1**) as well as aminoaciduria (**Fig. 2i**), were observed in 24-week-old *Atg7*$^{PT\text{-}KO}$ mice compared to CTR littermates. Despite impaired autophagy and PT dysfunction, no signs of fibrotic alterations (**Supplementary Fig. 2d**), activation of apoptosis (**Supplementary Fig. 2e,f top panel**), the release of damage markers (Lipocalin 2, Lcn2; **Supplementary Fig. 2f, bottom panel**), or interstitial inflammation (**Supplementary Fig. 2g-h**) were detected in the *Atg7*$^{PT\text{-}KO}$ kidneys. Blood urea nitrogen (BUN) and plasma creatinine (**Supplementary Fig. 2i,j; Supplementary Table 2**), and survival rates were similar between *Atg7*$^{PT\text{-}KO}$ mice and CTR littermates (**Supplementary Fig. 2k**). These data reveal that impairment of ATG7-dependent autophagy compromises the homeostasis of PT cells, leading to the development of a proximal tubulopathy in the absence of structural kidney damage.

***ATG7 deficiency diverts PT differentiation towards anabolic growth and proliferation***

Since ultrafiltered proteins enter PT cells through receptor-mediated endocytosis[5], we investigated whether the tubular proteinuria induced by ATG7 deficiency reflects changes in the endocytic activities of PT cells, using well-established tracers (**Fig. 3a**). The loss of ATG7-mediated autophagy significantly reduced lactoglobulin endocytosis in the kidney PT of *Atg7*$^{PT\text{-}KO}$ mice compared to their CTR littermates (**Fig. 3b**). Similarly, fluid-phase endocytosis, assessed after injecting Alexa647-labelled dextran, was also decreased in PT cells lacking ATG7/autophagy (**Fig. 3b**).

Given that apical endocytosis is a marker of terminal differentiation of PT cells[9,10,11], we examined whether defective ATG7-dependent autophagy impairs the functioning state of tubular epithelial cells by antagonising their differentiation trajectories. The deletion of *Atg7* significantly lowered the expression of PT cell-specific genes (*Slc34a2* and *Slc5a2*; **Fig. 3c**) and endocytic receptors (*Lrp2* and *Cubn*; **Fig. 3c**). It also impacted the apical recycling pathway of endocytic receptors in the PT cells[31], as evidenced by reduced levels of apical fast-recycling Lrp2/megalin and transferrin receptor (**Fig. 3d; Supplementary Fig. 3a**) – despite preserved expression of proteins of the endosomal and lysosomal pathways (**Supplementary Fig. 3b**). This was contrasted with an increased expression of genes involved in cell cycle regulation (*Ccna2*, *Ccnb2*, and *Cdc20*; **Fig. 3e**) and cell proliferation (*Pcna* and *Ki67*; **Fig. 3e,f**) in the PT of *Atg7*$^{PT\text{-}KO}$ mouse kidneys. Furthermore, mutant mice lacking ATG7/autophagy had increased kidney weight to body weight ratio (**Supplementary Fig. 3c**). Consistent with abnormal differentiation programs, PT cells from *Atg7*$^{PT\text{-}KO}$ mice displayed a transition from a cuboidal shape to columnar epithelium (**Supplementary Fig. 3d**). In contrast, the loss of ATG7-mediated autophagy did not result in any changes in the expression of nuclear receptors and transcription factors (*Esrra*, *Hnf1a*, *Hnf4a*, *Ppara*; **Supplementary Fig. 3e**) that couple PT metabolism to differentiation.[26] Also, the nuclear receptor co-repressor 1 (NCoR1), which interacts with PPARα to suppress its transactivation[32], did not increase in the PT segments of mutant mice (**Supplementary Fig. 3f**). Thus, the inactivation of ATG7/autophagy diverts the metabolic trajectories of PT cells towards anabolic programs for growth and proliferation, ultimately disrupting homeostasis, and their shape and nutrient seeking activities.

***Metabolic changes and dedifferentiation in PT cells lacking Atg7-mediated autophagy***

We next used an established primary PT cell-based culture system (mPTCs) to delve into the mechanisms of dysregulated homeostasis and dysfunction resulting from *Atg7* deletion (**Fig. 4a**). Compared to control cells, mPTCs isolated from *Atg7*$^{PT\text{-}KO}$ mouse kidneys displayed a significant decrease in the conversion of Map1Lc3b-I to Map1Lc3b-II and a

reduction in the number of Map1Lc3b-flagged autophagosomes under both fed and starvation-induced autophagy conditions, as well as in the presence of the autophagy flux inhibitor Bafilomycin A1 (BafA1; **Fig. 4b-f**). In agreement, transmission electron microscopy (TEM) revealed a marked reduction in the number of structures compatible with autophagic vesicles in starved, ATG7-deficient mPTCs treated with BafA1 (**Fig. 4g**). These alterations were accompanied by changes in the expression of endocytic receptors (**Fig. 4h**), defective dynamics of lysosomes and their catabolic activities (**Supplementary Fig. 4a,b**), abnormal growth and proliferation rates (**Fig. 4h-i**), and impaired endocytosis of fluorescent-labelled ligands (**Fig. 4j**), closely recapitulating the abnormalities observed in the PT of *Atg7*$^{PT\text{-}KO}$ mouse kidneys. The effects of *Atg7* loss on tubular cell phenotypes were not attributable to changes in the expression of other genes associated with autophagy machinery and the autophagosome formation (**Supplementary Fig. 4c**) or altered levels of the mechanistic target of rapamycin complex 1 (mTORC1) activity[33] (**Supplementary Fig. 4d**). Thus, defective ATG7-mediated autophagy leads to dysregulated homeostasis and dedifferentiation through mechanisms that are, at least in part, distinct from the mTORC1 signalling pathway.

***Loss of ATG7 disrupts the autophagy-mediated regulation of lipid metabolism***

To identify the factors driving dysregulated homeostasis downstream of ATG7 loss and impaired autophagy, we performed proteomic and metabolomic profiling of *Atg7*-deficient mPTCs, alongside pathway and network enrichment analyses. Principal component (PCA) and hierarchical clustering revealed substantial differences in the proteomes and metabolomes of *Atg7*$^{PT\text{-}KO}$ mPTCs compared to control cells (**Supplementary Fig. 5a-d**). Protein-protein interaction (PPI) network analysis showed significant enrichment of proteins associated with mitochondria and metabolic pathways, including amino acid and fatty acid metabolism, the TCA cycle, electron transport, fatty acid oxidation, and energy production in *Atg7*$^{PT\text{-}KO}$ mPTCs (**Supplementary Fig. 5e**). Metabolite set enrichment analysis (MSEA) identified organic acids, lipids, and nucleotides as dominant chemical categories in *Atg7*$^{PT\text{-}KO}$

cells (**Supplementary Fig. 5f**). Integrated biological network and pathway analysis, which crossed differentially produced proteins and metabolites, revealed enrichment of pathways linked to metabolism — such as fatty acid elongation and degradation, the TCA cycle, and amino acid metabolism — in *Atg7*$^{PT\text{-}KO}$ mPTCs compared to control cells (**Fig. 5a**). This aligns with increased anabolic activity driving growth and proliferation in these mutant cells. Additionally, clusters of proteins and metabolites linked to cellular degradation systems, including autophagy and lysosomes, were also identified in ATG7-deficient mPTCs (**Fig. 5a**). Moreover, we noted an enrichment in pathways related to senescence, renal cell carcinoma and cancer cell metabolism, known to be driven by dysregulated autophagy (**Fig. 5a**).[7,12] Building on this evidence, we hypothesised that loss of *Atg7* would impair the autophagy-mediated regulation of lipid homeostasis and metabolism. To test this hypothesis, we cultured *Atg7* mPTCs in nutrient-rich or nutrient-deprived conditions to stimulate the degradation and utilization of lipid droplets. Under nutrient withdrawal, wild-type cells responded by increasing lipid droplet storage, as visualised by Bodipy 493/503 staining (**Fig. 5b**). This aligns with prior studies showing the transfer of DGAT1-dependent fatty acids from autophagic degradation of organelles to lipid droplets.[34] In contrast, *Atg7*$^{PT\text{-}KO}$ mPTCs displayed a higher baseline number of lipid droplets, which did not increase further under starvation conditions (**Fig. 5b**). This suggests a defective regulation of lipid droplet stores in the absence of ATG7-mediated autophagy. Substantiating these metabolic abnormalities, quantitative lipidomics revealed elevated levels of triglycerides and phosphatidylcholines, alongside changes in lysophosphatidylethanolamine and sphingomyelin levels in *Atg7*-deficient mPTCs compared to control cells (**Fig. 5c; Supplementary Fig. 6a-d**). Inhibiting lysosomal degradation (via BafA1), blocking mitochondrial fatty acid oxidation (using Etomoxir), or suppressing autophagy initiation (via the class III phosphatidylinositol 3-kinase inhibitor SAR405), impaired lipid droplet degradation, as indicated by increased lipid droplet stores in ATG7-competent cells (**Supplementary Fig. 7a,b**), in line with the role of autophagy in lipid droplet catabolism and homeostasis.[35]

Despite the storage of lipid droplets in autophagy-incompetent cells, we observed no significant changes in the expression of genes regulating fatty acid transport, peroxisomal and mitochondrial fatty acid oxidation, and *de novo* lipogenesis (**Supplementary Fig. 7c**) in *Atg7*$^{PT\text{-}KO}$ mPTCs compared to control cells. Furthermore, there were no differences in the clearance of mitochondrial proteins (**Supplementary Fig. 8a**) in mutant cells. However, we did observe a decrease in the number of Vdac1$^{+}$ mitochondria in the kidney PT and an increase in mitochondrial proteins (Cox IV and Sdha) in the urine samples of *Atg7*$^{PT\text{-}KO}$ mice compared to their CTR littermates (**Supplementary Fig. 8b,c**), suggesting the existence of compensatory mitochondrial quality control (MQC) pathways that secrete damaged mitochondria in the absence of canonical ATG7-mediated autophagy.[36] Lastly, dysregulated lipid droplet metabolism in ATG7-deficient mPTCs was not driven by alterations in transcriptional programs governing mitochondrial biogenesis or dynamics (**Supplementary Fig. 8d**). Thus, the absence of ATG7 impairs the autophagy-mediated regulation of lipid droplet homeostasis, impairing metabolic homeostasis and physiological functions.

***Defective autophagy impairs mitochondrial metabolism and energy production***

The breakdown of lipid droplets releases fatty acids that are transported to mitochondria for β-oxidation and energy production.[35] To investigate whether ATG7-mediated autophagy is essential for this process, we tracked the movement of the green-fluorescent FA derivative Bodipy C16 (Green-C16) to mitochondria in *Atg7*$^{PT\text{-}KO}$ mPTCs compared to wild-type cells. This fluorescent fatty acid is incorporated into lipid droplet-specific neutral lipids and then metabolised by mitochondria for β-oxidation and energy production. Following a 16-hour pulse and a 16-hour chase in nutrient-rich media (NRM), confocal microscopy combined with semi-automated image analysis was used to quantify fatty acid transport to mitochondria (**Fig. 5d**). In control cells, Green-C16 was efficiently transported to mitochondria (**Fig. 5e**). Conversely, in *Atg7*$^{PT\text{-}KO}$ mPTCs, Green-C16 remained largely in lipid droplet stores with minimal transfer to mitochondria, indicating dysregulated fatty acid efflux and reduced mitochondrial lipid availability (**Fig. 5e**). This was corroborated by Seahorse-based analysis

of cellular respiration, which revealed a significant reduction in both basal, ATP production-linked oxygen consumption rate (OCR), and maximal respiration in ATG7-deficient mPTCs compared to control cells (**Fig. 5f**). Mitochondrial membrane potential was also reduced, as evidenced by lower mean fluorescence intensity of the active mitochondria-labelling dye TMRM in PT cells lacking ATG7 and autophagy (**Fig. 5g; Supplementary Fig. 8e**). Additionally, the loss of ATG7 resulted in a marked increase in mitochondrial reactive oxygen species (mt-ROS), as evidenced by the mitochondrial ROS indicator MitoSOX (**Fig. 5h; Supplementary 8f**). The deficiency of ATG7 disrupts autophagy-mediated lipid droplet degradation, reducing the availability of fatty acids to mitochondria for oxidative metabolism and energy production. Consequently, PT cells steer their metabolic trajectories towards anabolic growth and proliferation, leading to dedifferentiation and altered reabsorptive activities. Enhancing fatty acid oxidation (FAO) with fenofibrate (a PPAR-α agonist) significantly increased the endocytosis of fluorescent-tagged ligands in ATG7/autophagy-deficient cells (**Supplementary Fig. 8g)**. In contrast, non-toxic low-doses of Etomoxir reduced ligand endocytosis in ATG7/autophagy-competent PT cells (**Supplementary Fig. 8g**). Together these results suggest that ATG7-driven autophagy regulates lipid metabolism to sustain PT intense bioenergetic demands and physiology.

**Cell-autonomous role of ATG7 in differentiation and metabolic homeostasis**

To confirm the cell-autonomous nature of the abnormal phenotype, we cultured PT cells from microdissected PT segments of *Atg7*$^{flox/flox}$ mouse kidneys (**Fig. 6a**). Transduction of *Atg7*$^{flox/flox}$ mPTCs with adenovirus particles carrying Cre-recombinase significantly reduced both *Atg7* mRNA and protein levels (**Fig. 6b; Supplementary Fig. 9a**). The loss of *Atg7* in PT cells impaired autophagy, as evidenced by decreased conversion of Map1Lc3b-I to Map1Lc3b-II, a reduction of the number of Map1Lc3b-flagged autophagosomes, and accumulation of the autophagy receptor Sqstm1. These effects were observed under both fed and starvation-induced autophagy conditions, as well as in the presence of the autophagy inhibitor BafA1 (**Fig. 6c,d; Supplementary Fig. 9b**). These changes closely

mirrored those observed in the *Atg7*$^{PT\text{-}KO}$ mouse kidneys and derived mPTCs. In line with defective autophagy-mediated quality control, *Atg7*-deleted mPTCs exhibited mitochondrial abnormalities, both in morphology and bioenergetics, compared to control cells (**Fig. 6e-g**). These defects were linked to abnormal growth and proliferation rates (**Fig. 6h**), disrupted expression of PT-cell-specific genes and (de)differentiation markers (**Fig. 6i,j**), and reduced endocytosis of fluorescent-tagged ligands (**Fig. 6k; Supplementary Fig. 9c,d**). Notably, similar phenotypes were observed in PT cells depleted of *Atg5* – another key regulator of autophagy initiation and autophagosome formation (**Supplementary Fig. 10a-e;** ref.12). Previous studies have identified non-canonical functions for certain autophagy proteins in alternative trafficking pathways, such as LC3-associated phagocytosis (LAP[37]) and endocytosis (LANDO[38]). Knockout of *Fip200* – a protein essential for autophagy but not for LAP or LANDO – significantly impaired the endocytosis of fluorescent-tagged ligands in mPTCs (**Supplementary Fig. 10c,f,g,h)**, highlighting the central role of autophagy in PT cell differentiation and homeostasis.

***Metabolic and functional conservation of ATG7 in nematodes and zebrafish***

We tested whether the biological functions of ATG7-mediated autophagy are evolutionarily conserved. In the nematode *Caenorhabditis elegans*, we utilized two well-established markers[39] — SQST-1::RFP to assess autophagy levels and DHS-3::GFP to track intestinal lipid droplets (**Fig. 7a**). Loss of *atg7* elevated levels of the autophagy marker SQST-1 (**Fig. 7b**) and resulted in lipid droplet accumulation in the intestine during early adulthood (**Fig. 7c**). This was accompanied by decreased mitochondrial bioenergetics via reduced whole-organism respiration (**Fig. 7a,d**), demonstrating the evolutionary conservation of this metabolic connection. Given the absence of kidney PT-like structures in *C. elegans*, we turned to zebrafish (*Danio rerio*) to explore the biological role of atg7/autophagy. The zebrafish pronephros closely mirrors the architecture of mammalian kidneys, featuring junctional complexes, a well-developed endolysosomal system, mitochondria-driven energy metabolism, endocytic receptors, and nutrient transporters.[40,41] We generated a whole-body

deficiency of *atg7* in zebrafish using CRISPR/Cas9 genome editing, resulting in a 6bp/2bp deletion/insertion in *atg7*, producing a truncated, non-functional protein (**Supplementary Fig. 11a,b**). The specificity of *atg7* deletion in mutant zebrafish (hereafter referred to as *atg7*$^{KO}$) was verified through RT-qPCR analysis (**Supplementary Fig. 11c**). While *atg7*$^{KO}$ zebrafish larvae display no lethality at birth or morphological defects during development (**Supplementary Fig. 11d**), their survival rate dropped significantly, with high mortality observed by 20 days post-fertilization (dpf; **Fig. 8a**). Investigations were therefore performed using mutant zebrafish aged 4- and 19-dpf. Behavioural analysis revealed shorter swimming distances in *atg7*$^{KO}$ zebrafish compared to wild-type larvae starting at 14 dpf (**Fig. 8b,c**). To assess autophagy in the pronephros, we developed a transgenic reporter line expressing the mCherry-tagged autophagosome marker, microtubule-associated protein light chain 3B (mCherry-MAP1LC3B, **Fig. 8d**). When crossed to heterozygous *atg7*-deficient zebrafish, the number of mCherry-MAP1LC3B-tagged autophagosomes was significantly reduced in the pronephros of *atg7*-deficient zebrafish compared to wild-type larvae (**Fig. 8e; Supplementary Fig. 11e**). Electron microscopy confirmed this defect, showing cup-shaped phagophore structures and disrupted autophagic vacuoles in the pronephros of *atg7*-deficient zebrafish larvae (**Supplementary Fig. 11f**).

To determine whether the inactivation of atg7-dependent autophagy triggers pronephros dysfunction, we monitored the excretion of LMW proteins in wild-type and *atg7*-deficient zebrafish expressing an LMW proteinuria biosensor[41](*lfabp10a::½ vdbp-mCherry*; **Fig. 8f and Supplementary Fig. 11g**). At 14-dpf, the *atg7*-deficient zebrafish exhibited significant increases in LMWP/mCherry levels in their urine compared to their age-matched wild-type larvae (**Fig. 8g**). Re-introducing human wild-type ATG7 rescued the pronephros dysfunction and reduced tubular proteinuria in *atg7*$^{KO}$ zebrafish (**Fig. 8h; Supplementary Fig. 11h**). Conversely, pharmacological inhibition of mitochondrial fatty acid oxidation using low, non-toxic doses of Etomoxir impaired swimming behaviour (**Fig. 8i**) and induced tubular proteinuria in *atg7*/autophagy-competent zebrafish (**Fig. 8j**). Taken together, these findings highlight an evolutionarily conserved role of ATG7-driven autophagy in regulating the

metabolic trajectories of specialized epithelial cells and sustaining their homeostatic functions.

***Association of ATG7 variants with human kidney disease phenotypes***

Our studies in model systems underscore the importance of ATG7 for the function and metabolic characteristics of specialised kidney tubular epithelial cells. While autophagy dysfunction has been implicated in human disorders[7,12,18], no association between variants in the human *ATG7* gene and kidney-related diseases has been reported thus far. Utilizing phenome-wide genetic association meta-analysis across multiple populations (635,969 participants, VA Million Veteran Program[42]), we noted a genome-wide significant signal ($P$=2×10$^{-11}$) associated with a rare intronic variant, rs375156407 (minor allele frequency, MAF = 0.06%), located within the *ATG7* locus (**Supplementary Fig. 12a,b**). This variant was linked to various kidney-related disease conditions (**Fig. 9a,b**), in line with prior evidence showing the involvement of individual autophagy genes in disease as causative or risk factors.[7,12,43] Notably, we identified an association between the *ATG7* locus and various traits, including blood pressure regulation and hypertension — conditions causing or originating from kidney damage — and height, the most heritable trait across ancestries[42], in line with the crucial role of autophagy in health and homeostasis.[7,12,43] Similarly, Human Genetic Evidence (HuGE) scores from the Common Metabolic Diseases Knowledge Portal (https://md.hugeamp.org/) revealed associations between *ATG7* and traits related to kidney function (e.g., blood urea nitrogen, eGFR creatinine, and cystatin C), liver function and red blood cell indices, and insulin like-growth signalling and lipid biology (**Supplementary Fig. 12c**). Together these findings further substantiate the role of ATG7 in homeostasis and human health.

A recent study identified individuals from five unrelated families with pathogenic, biallelic *ATG7* variants, leading to impaired autophagy and a variable neurodevelopmental disorder.[29] Among them, two adult female siblings (P1 and P2) were compound heterozygous for segregating loss-of-function *ATG7* variants (NM_--6395.2: c.1975C>T (p.Arg659*); c.2080-

2A>G; RefSeq accession number, NM_006395.2), leading to complete loss of immunodetectable ATG7 protein in different tissues using N- and C-terminal antibodies.[29] This prompted us to test whether a congenital lack of ATG7 is also linked to tubular proteinuria in humans. Analysing urine samples from P1 and P2 individuals, we did not detect standard markers of tubular proteinuria (retinal binding protein) or aminoaciduria; however, we could detect increased urinary levels of LMW proteinuria marker CC16 in P2, compared to P1 and age-and gender-matched healthy controls (**Fig. 9c**). Metabolomics-based profiling on baseline and 1-year follow-up urine samples from P2 and P1 individuals (**Fig. 9d**) revealed substantial metabolomic differences between P2 and P1 and between the two siblings and healthy controls (**Supplementary Fig. 13a-c**). Analysis of differentially produced metabolites revealed significant enrichment of pathways associated with glucose, amino acid and nucleotide metabolism, fatty acid degradation, the TCA cycle, and cancer metabolism in P2 compared to the P1 subject (**Fig. 9e**), reminiscent of metabolic abnormalities encountered in preclinical models of ATG7/autophagy deficiency.

**Low ATG7 levels, dedifferentiation, and poor prognosis in renal cell carcinoma**

Clear cell renal cell carcinoma (ccRCC) – the most common type of kidney cancer – originates from PT epithelial cells and is characterized by the hallmark accumulation of lipid droplets.[44,45] Given the enrichment of pathways related to renal cell carcinoma and cancer metabolism in mouse cells and human urine samples, alongside lipid droplet storage in mPTCs lacking ATG7 and autophagy, we investigated the potential involvement of ATG7 in renal cell carcinoma. Using exome-based association studies from 394,841 individuals from the UK biobank[46], we unveiled an association between the burden of putative loss-of-function *ATG7* variants and a higher incidence of malignant neoplasms of the kidney (ICD-10 code C64; p-value=$2.16e^{-04}$, beta coefficient=0.097; **Supplementary Fig. 14a**). We further analysed data from the KIRC/ccRCC cohort in The Cancer Genome Atlas (TCGA).[47] Stratification of KIRC/ccRCC patients by ATG7 expression levels in primary tumours (low expression tertile vs. medium/high tertiles, relative to adjacent non-cancerous kidney tissues;

Fig. 10a) revealed a significant correlation between low ATG7 expression and reduced overall survival, as demonstrated by Kaplan-Meier survival analysis ($p=2.23e^{-02}$; Fig. 10b). To investigate the biological role of ATG7 in renal cell carcinoma, we queried publicly available bulk RNA sequencing and microarray data. A meta-analysis was performed using six datasets, comprising data from 146 healthy controls and 656 patients with KIRC/ccRCC (Fig. 10c). We found that proliferation and dedifferentiation markers were strongly upregulated (combined q-value < 0.001, except *SOX9*, combined q-value = 0.89), while PT-specific genes were consistently downregulated in tumour samples (combined q-value < 0.001; Fig. 10d). Finally, we used the publicly available single-cell RNA sequencing (scRNA-seq) datasets from two untreated patients with ccRCC to evaluate potential changes in *ATG7* expression in specific cell types.[48] Comparison of tumour and adjacent normal kidney tissue data revealed 31 distinct cell clusters, including immunocytes and renal epithelium cells (Supplementary Fig. 14b). While *ATG7* expression was broadly detected across cell populations, it was significantly reduced in PAX8-positive renal epithelial cells within tumour samples compared to control tissues (LFC= -1.20, p-value=0.05; Fig. 10e). This reduction was especially pronounced in untreated patient 2 (LFC = -1.53, p-value = 0.03), who exhibited a higher proportion of tumour cells relative to untreated patient 1 (Fig. 10e; Supplementary Fig. 14b,c). Set enrichment analysis of differentially expressed genes (DEGs) showed that tumour epithelial cells in untreated patient 2 exhibited pathway dysregulation resembling abnormalities seen in ATG7-deficient PT cells, including upregulation of epithelial-to-mesenchymal transition and downregulation of nutrient endocytosis and transport, mitochondrial metabolism, and epithelial integrity (Supplementary Fig. 14d,e). Taken together, these results indicate that ATG7 loss and autophagy dysfunction can drive metabolic reprogramming and PT dedifferentiation, contributing to the progression of ccRCC and reduced overall survival in patients.

## Discussion

The precise coupling between nutrient metabolism and physiology is crucial for maintaining cell and organ homeostasis. This study underscores the critical role of ATG7-mediated autophagy in preserving the differentiation and homeostatic functions of specialized epithelial cells lining the kidney tubule. The deficiency of ATG7 disrupts autophagy, reprogramming the metabolic trajectories of PT cells toward anabolic growth and proliferation at the expense of their specialized transport and nutrient-reabsorbing activities. This leads to proximal tubulopathy, evidenced by the urinary loss of essential nutrients and solutes. Mechanistically, the maintenance of ATG7-mediated autophagy coordinates lipid droplet lipolysis and mitochondrial fatty acid metabolism in nematodes and mice, ensuring adequate energy supply to fuel ATP-dependent transport and the homeostatic functions of specialized cell types. Restoring wild-type ATG7 in a zebrafish model of ATG7/autophagy deficiency reinstates the nutrient-reabsorbing activities of the pronephric kidneys and alleviates proximal tubulopathy. Strikingly, abolishing mitochondrial fatty acid metabolism disrupts homeostatic functions in atg7/autophagy-competent zebrafish, highlighting the evolutionary conservation of this metabolic-function connection. Our work also provides genetic evidence supporting the critical role of ATG7-driven autophagy in homeostasis, with implications for human health and disease.

By integrating cell-type specific genetic perturbation with high-resolution live imaging and physiological assays, our work reveals that PT cells lacking ATG7 exhibit profound defects in their catabolic trajectories, with an accumulation of cellular components, such as defective organelles (mitochondria) and p62/Sqstm1$^{+}$ aggregates of misfolded proteins, which are normally dismantled through autophagy.[7,12] These changes coincide with the abnormal activation of anabolic programs for growth and proliferation, and altered differentiation states of PT cells. In turn, the latter impairs receptor-mediated endocytosis and other transport processes, leading to proximal tubulopathy and excessive loss of nutrients. Thus, beyond its canonical role in autophagy, ATG7 emerges as a key metabolic

regulator, orchestrating the balance between catabolic and anabolic processes to sustain the specialized functions of PT cells.

The PT dysfunction observed in *Atg7*$^{PT\text{-}KO}$ mice closely mirrors the perturbations seen in various inherited proximal tubulopathies, including abnormal activation of lysosomal growth signalling pathways and impaired receptor-mediated endocytosis.[3,4,8,9,10,11] Deletion of *Atg7* significantly decreases the expression of PT cell-specific genes and the recycling of endocytic receptors, which are critical coordinators of protein reabsorption in PT segments of the kidney.[5] Additionally, *Atg7* deficiency reduces the abundance of nutrient transporters, impairing the reabsorption of other ligands such as glucose, amino acids, and other solutes.

Previous studies have identified non-canonical roles for a subset of autophagy proteins[49], including ATG7, in alternative trafficking pathways such as LC3-associated phagocytosis (LAP[37]) and endocytosis (LANDO[38]). Further experiments designed to fully uncouple autophagic versus non-autophagic activities reveal that knockdown of *Fip200*, which is required for autophagy but not for LAP or LANDO, compromises the endocytosis/reabsorptive activities of PT cells. This phenotype closely mirrors the deficits observed in ATG7-deficient PT cells, underscoring the biological role of autophagy in nutrient acquisition strategies and homeostasis.

Similar to the alterations observed in mouse kidneys, the zebrafish pronephros lacking *atg7* displays a markedly reduced number of autophagosomes and impaired autophagy biogenesis. This deficiency results in defective reabsorption of filtered proteins, leading to their loss in the urine. Moreover, atg7/autophagy incompetent zebrafish exhibit swimming defects and behavioural phenotypes, which correlate with excessive larval lethality. These findings are in line with prior studies indicating that zebrafish lacking upstream *atg* genes die earlier than those lacking genes encoding *atg* conjugation system components, as observed in *Atg*-deficient mice.[12,14-16] Functional complementation studies through the reintroduction of human wild-type ATG7 into atg7/autophagy-incompetent zebrafish effectively mitigates PT dysfunction and proximal tubulopathy, substantiating the role of ATG7 in the maintenance of cellular homeostasis and organ physiology in an evolutionarily conserved manner.

How does the inactivation of ATG7-directed autophagy compromise the reabsorptive activities of PT cells and their homeostatic functions? Tubular cells have high energy demands, primarily relying on oxidative phosphorylation driven by fatty acid oxidation (FAO) for energy production, which predominantly occurs within the mitochondria.[24,25] Therefore, maintaining healthy mitochondria is crucial for sustaining the intense transport processes in PT cells and their homeostatic functions. Prior evidence indicates that autophagy plays a pivotal role in this process by selectively tagging, removing, and recycling damaged and depolarized mitochondria.[7,12,18] This quality-control mechanism preserves optimal levels of mitochondrial metabolic activities, such as oxidative phosphorylation and ATP synthesis, which are essential for the bioenergetic demands of the tubular epithelial cells.[21,24,26] Accordingly, steady-state levels of autophagosomes and their increased induction has been observed in the kidneys of GFP-LC3B autophagy reporter mice.[20,21] Our integrative multi-omics analyses, combined with cross-species validation in nematodes and mammalian cells, reveal that inhibiting ATG7-mediated autophagy leads to the storage of fatty acids in lipid droplets, reducing their flux into the mitochondria for energy metabolism. These findings confirm that lipid droplets are degraded through autophagy[35], underlying the pivotal role of ATG7 in lipid metabolism and metabolic homeostasis.

Defective lipid droplet homeostasis caused by impaired ATG7/autophagy disrupts the transfer of fatty acids to mitochondria, limiting their utilization and leading to reduced ATP production and energy metabolism. Consistently, tubular cells deficient in ATG7/autophagy display fragmented mitochondria, decreased mitochondrial membrane potential, and impaired bioenergetics. These alterations are accompanied by increased oxidative stress, indicating dysfunctional and/or damaged mitochondria. Prior studies have shown that defective autophagy-mediated turnover of damaged mitochondria disrupts the metabolic profile of tubular cells, driving cell-fate transitions and dedifferentiation in cystinosis[3,10,11] — a lysosomal storage disease characterized by PT cell dysfunction and proximal tubulopathy. Additionally, because ATG7 loss and autophagy dysfunction changes in the expression of genes associated with PT cell function and differentiation, additional layers of (dys)regulation

are likely involved. Thus, ATG7 may function not only as a core component of autophagy machinery but also as a metabolic rheostat coordinating cell-fate decisions and specialization, as recently described for other autophagy proteins[50,51], including ATG9 and ATG14.

Our findings provide both observational and genetic evidence underscoring the critical role of ATG7-mediated autophagy in homeostasis and its contribution to kidney disease development and progression. First, phenome-wide genetic associations conducted on large, multi-ancestry population cohorts link the *ATG7* locus to an increased risk of kidney disease. Second, deep phenotyping of ATG7 dysfunction in a family with deleterious, biallelic *ATG7* variants[29] revealed alterations in mitochondrial metabolic pathways and evidence of tubular proteinuria in one affected sibling. Such subtle kidney abnormalities, which may be missed in routine clinical testing, suggest the presence of compensatory mechanisms mitigating the effects of ATG7 loss in humans.[52] Third, we establish a clinical correlation between low ATG7 expression and poorer outcomes in patients with ccRCC, the most common form of kidney cancer originating from PT cells.[44,45] This correlation is characterized by the upregulation of epithelial-to-mesenchymal transition and the downregulation of pathways related to PT differentiation and energy metabolism, processes known to be implicated in ccRCC progression and metastasis.[44,45] These changes mirror the phenotypes observed in preclinical models of *Atg7* deficiency and cystinosis[11], exhibiting metabolomic and proteomic signatures reminiscent of renal cell carcinoma. Thus, the maintenance of autophagy links oxidative energy metabolism to kidney tubular epithelial cell fate specialization and differentiation, with its disruption contributing to disease development or being exploited by malignant cells during tumour progression.

In summary, our work describes the critical role of ATG7-mediated autophagy as a metabolic determinant of kidney tubular epithelial cell fate specialisation and differentiation – with relevance across the spectrum of health and disease. Together, these findings provide actionable insights into the fundamental mechanisms of homeostasis, offering potential therapeutic targets for addressing currently intractable disorders.

## MATERIAL AND METHODS

**Ethical compliance.** All the animal experiments were approved by the Cantonal Veterinary Office Zurich (license no. ZH195/2020 and ZH139/2022) and performed following the guidelines of the University of Zurich.

**Human studies.** Patients with an established diagnosis of ATG7-related spinocerebellar ataxia (MIM #619422), i.e. with biallelic pathogenic *ATG7* variants were recruited (Family 1; ref. 29). Written informed consent was obtained from the parents of the siblings in the study and controls following the Declaration of Helsinki protocols, and the experimental protocol was approved by the local institutional review board. Urine samples were collected in the morning and kept at 4°C before it was frozen at -80 °C. For immunoblot analysis, the loading volume was indexed to creatinine to correct for variations in urine concentration. Urinary creatinine levels were measured using UniCel DxC 800 proSynchron (Beckman Coulter, Fullerton, CA, USA), according to manufacturer instructions.

**Antibodies and reagents.** The following antibodies were used in this study: rabbit anti-Atg7 (Sigma-Aldrich, A2856; 1:200); rabbit anti-Apg5l/Atg5 (Abcam, 108327, 1:500); mouse anti-AQP1(Abcam, ab9566, 1:400); mouse anti-β-actin (Sigma-Aldrich, A5441, 1:1000); rabbit anti-cleaved caspase 3 (Cell Signaling), 9662, 1:400); rabbit anti-caspase 3 (Cell Signaling, 9661, 1:400); rabbit anti-phospho-4E-BP1 (Ser65; Cell Signaling technology, 9451, 1:500); rabbit anti-4E-BP1 (Cell Signaling Technology, 9644, 1:500);rabbit anti-FIP200 (Cell Signaling, 12436S, 1:200); sheep anti-Lrp2/megalin (1:1000) was kindly provided by P. Verroust and R. Kozyraki (INSERM, Paris, France); rabbit anti-Laminin gamma 1 (clone A5; Thermo Fisher Scientific, MA5-14649, 1:400); rat anti-LAMP1 (Santa Cruz Biotechnology, sc-19992, 1:1000); rabbit anti-LC3 (PM036, MBL, 1:200); rabbit anti-NCoR1 (Cell Signaling S9448S; 1:500); anti-PPARα (Abcam 126289: 1:500); mouse anti-PCNA (Dako, M0879, 1:500); rabbit anti-Rab5 (Abcam, ab218624; 1:500); rabbit anti-Rab7 (Abcam, ab137029; 1:500); mouse anti-SQTM1 (Abcam, ab56416; 1:500); rabbit anti-SQTM1 (Abcam,

ab109012; 1:400); mouse anti-transferrin receptor (H68.4) (Thermo Fisher Scientific 13-6800; 1:400); human anti-Transferrin (Dako, A0061; 1:500); mouse anti-TOM20 (Abcam; ab186735; 1:400); rabbit anti-uteroglobin (also known as CC16, Abcam, ab40873; 1:500); sheep anti-uromodulin (K90071C, Meridian Life Science Inc., Cincinnati, OH, USA; 1:300); donkey-anti rabbit IgG, cross-absorbed secondary antibody, Alexa Fluor 488 (Thermo Fischer Scientific, A10040, 1:400); goat-anti mouse IgG, cross-absorbed secondary antibody, Alexa Fluor 633 (Thermo Fischer Scientific, A21052, 1:400); goat-anti mouse IgG, cross-absorbed secondary antibody, Alexa Fluor 546 (Thermo Fischer Scientific, A11003, 1:400); goat-anti rat IgG, cross-absorbed secondary antibody, Alexa Fluor 633 (Thermo Fischer Scientific, A21094, 1:400); donkey-anti goat IgG, cross-absorbed secondary antibody, Alexa Fluor 633 (Thermo Fischer Scientific, A21094, 1:400); donkey-anti sheep IgG, cross-absorbed secondary antibody, Alexa Fluor 633 (Thermo Fischer Scientific, A21100, 1:400). Compounds included Bafilomycin A1 (BafA1; Enzo Life Sciences, ALX-380-030, 250 nM), the biotinylated Lotus Tetragonolobus Lectin (LTL; Vector Laboratories, B-1325), and 4′,6-diamino-2-phenylindole dihydrochloride (DAPI; D1306, Thermo Fischer Scientific; 1:1000), Etomoxir (Merck; 23620), and Fenofibrate (Sigma Aldrich; F620), and the PIK3C3/Vps34 inhibitor SAR-405 (A8883, APExBIO). All molecules were of at least 98% purity and dissolved in dimethylsulfoxide (DMSO) for experiments unless specified. The cells used in this study were negatively tested for mycoplasma contamination using MycoAlert™ Mycoplasma Detection Kit (LT07-118, Lonza, Switzerland).

***C. elegans* strain maintenance.** For all experiments using invertebrate *C. elegans*, hermaphroditic animals were used (wild-type and *atg7* mutant). Worms from mutant deletion strains were genotyped by PCR, and the PCR amplicon sizes were used to check for the presence of the deletion. The ages of adult animals are specifically defined in figures and figure legends. The nematodes were raised at 20 °C on nematode growth medium (NGM) agar (51.3 mM NaCl, 0.25% peptone, 1.7% agar, 1 mM $CaCl_2$, 1 mM $MgSO_4$, 25 mM $KPO_4$ and 12.9 μM cholesterol, pH 6.0). Fed worms were maintained on NGM agar plates that had

been seeded with *Escherichia coli* OP50 bacteria. Synchronous populations of worms were obtained by bleaching young adult hermaphrodites. Briefly, adult hermaphrodites were exposed to 1 mL bleaching solution (0.5 M NaOH and 20% bleach) for 5 min to isolate eggs, and eggs were then washed three times in M9 buffer (22 mM $KH_2PO_4$, 42 mM $Na_2HPO_4$, 85.5 mM NaCl and 1 mM $MgSO_4$) before plating.

**Quantification of lipid droplets and autophagy in *C. elegans*.** To visualize lipid droplets, we utilized a reporter strain expressing DHS-3 fused to GFP [LIU1: (N2; ldrIs1 (dhs-3p::dhs-3::GFP; unc-76+)], LRL262: [*atg-7(bp411)*; ldrIs1 (dhs-3p::dhs-3::GFP; unc-76+)], a well-established marker for lipid droplets in *C. elegans*.[39] DHS-3 is orthologous to the mammalian 17β-HSD11 and is among the most abundant lipid droplet-associated proteins identified via mass spectrometry in *C. elegans*.[53,54] Its localisation to the lipid droplet membrane was confirmed through fluorescence microscopy. To visualize autophagy, we employed a reporter strain expressing SQST-1 fused to RFP [(LRL160: [N2; llcIs12 (p62p::p62::RFP::unc-54 3'UTR; myo-2::GFP)] and LRL256: [*atg-7(bp411);* llcIs12 (p62p::p62::RFP::unc-54 3'UTR; myo-2::GFP)], which is orthologous to the mammalian autophagy receptor SQSTM1/p62. Imaging was performed on day 3 or 4 of adulthood. Approximately 10 worms were imaged per condition for each experiment. Worms were mounted on a 2% agar pad, anaesthetised with 50 mM sodium azide, and covered with a glass coverslip for imaging. Confocal images were captured using an Olympus Fluoview FV3000 microscope equipped with the FV316-SW software (version 2.3.2.169). A 60% oil objective (UPLAN 60x oil, 2.35NA Olympus, Japan) and a 1.90-μm pinhole (resulting in an optical section thickness of 2.2 μm) were used. SQST-1::RFP reporter strain imaging was performed using a Zeiss V20 Discovery microscope equipped with an AxioCam 820 mono camera, Achromat S 1.0x FWD 63mm objective, and the Zeiss Zen 3.8 software. Imaging conditions, such as laser power and exposure time, were kept consistent across all samples. The mean fluorescence intensity was quantified using Fiji (version 2.0.0) by applying uniform thresholds to all images for consistency.

**Oxygen consumption measurements in *C. elegans*.** Worms were synchronized using a standard hypochlorite treatment protocol. Eggs were placed on OP50-seeded NGM plates and grown to day 2 of adulthood. Adult worms were hand-picked and transferred to P10 plates to control population density, with two plates containing 500 worms each and two plates containing 250 worms each. Worms were allowed to acclimate at 20°C for 30 minutes to minimize stress before measurements. Worms were harvested by rinsing the plates twice with 7 mL of M9 buffer, ensuring thorough collection. The suspensions were centrifuged at 1,000 rpm for 90 seconds, and the supernatant was discarded. Worms were washed three times with 13 mL of M9 buffer to eliminate residual bacteria and debris. After the final wash, 100 μL of the worm suspension was transferred into a pre-calibrated Oroboros chamber using a Pasteur pipette, ensuring minimal loss and preventing worms from adhering to surfaces. Oxygen consumption was continuously monitored using the Oroboros O2k system. Measurements were recorded until the nematodes exhibited signs of mortality. Data were normalized to the initial number of worms introduced into the chamber. All analyses were conducted using DatLab software.

**Generation and maintenance of *atg7* zebrafish.** The pT7-gRNA and pT3TS-nCas9n plasmids were sourced from Addgene (#46759 and #46757, respectively). To monitor CRISPR-Cas9-mediated mutations and facilitate genotyping, we selected the CRISPR-Cas9-targeted region (5′-GGCGAACTGAAGCTTCAGACTGG-3′), which contains the HindIII restriction site (AAGCTT). Oligonucleotides containing the sgRNA-targeting sequence were annealed and cloned into the Esp3I (BsmBI)-digested *pT7-gRNA* vector, resulting in *pT7-gRNA-atg7*. The oligonucleotide sequences were CRISPR-atg7-S: 5′-TTAGGCGAACTGAAGCTTCAGAC-3′ and CRISPR-atg7-AS: 5′-AAACGTCTGAAGCTTCAGTTCG-3′. Cas9 messenger RNA was produced by utilizing the XbaI-linearized *pT3TS-nCas9n* vector with the mMESSAGE T3 kit (Invitrogen). Both sgRNA-*atg7* and Cas9 mRNA were co-injected into one cell stage AB zebrafish embryos (*Danio rerio*). Genomic DNA was extracted from 2 dpf embryos that developed normally to detect

CRISPR-Cas9-induced mutation. Mosaic AB embryos injected with CRISPR-Cas9 were raised to adulthood (F0) and outcrossed with wild-type AB zebrafish. The resulting embryos (F1) were raised to adulthood, and heterozygous carriers were screened. We identified a heterozygous carrier with the mutation of 6bp-deletion + 2bp insertion (*atg7*$^{+/del4}$), and subsequent generations (F1) were crossed to obtain homozygous mutants carrying *atg7*$^{del4/del4}$. The CAS-OFFinder analysis confirmed that there were no off-target edits in other genes.[55] Zebrafish larvae (AB background) were maintained on a 14/10 h day/night cycle at 28°C and fed a standard diet (Zebrafeed 100-200, SPAROS, Portugal) from 5 dpf. Experiments were primarily conducted on larvae aged 5-14 dpf, with animal sex not specified at this developmental stage. Stable zebrafish lines expressing mCherry-tagged half vitamin D binding protein (½vdbp-mCherry) in the liver or hMAPLC3B in the kidney were established. These lines were subsequently outcrossed with *atg7*$^{+/del4}$ zebrafish to generate a transgenic mutant line. The latter was further crossed with *atg7*$^{+/del4}$ zebrafish to produce homozygous larvae. The measurement of ½vdbp-mCherry and mCherry-hMAPLC3B-flagged autophagic vesicles was assessed by ELISA and light sheet microscopy, respectively.

**Complementation studies in zebrafish.** For the generation of transgenic lines with a proximal tubule-specific expression of human *ATG7*, multisite Gateway cloning technology was used to generate the expression vector *PiT1::EGFP-hATG7* using plasmids coming from Tol2 kit v1.2. The cloning of the promoter of the zebrafish phosphate transporter 1/*slc20a1a* (*p5E-PiT1*) genes was previously described.[10,11] Human *ATG7* cDNA was amplified from the vector *pCMV-myc-ATG7* (kindly provided by Toren Finkel (Addgene plasmid # 24921)) and subcloned into *pENTR/D-TOPO vector* (Invitrogen) after N-Terminal Tagging with EGFP. The final expression vector *PiT1::EGFP-hATG7* was realized after LR Reaction (Gateway LR Clonase II Enzyme Mix, Invitrogen), which utilizes the LR clonase for vector construction through plasmids *p5E-PiT1*, *pED-EGFP-hATG7*, *p3E-polyA* and destination vector *pDestTol2CG2* with *cmlc2::EGFP* transgenesis marker. Plasmid DNA of

*PiT1::EGFP-hATG7* vector was co-injected with Tol2 transposase mRNA into zebrafish embryo at the one-cell stage to generate a stable transgenic line. Zebrafish *atg7*$^{+/del4}$, *Tg(PiT1::EGFP-hATG7)* was generated after crossing the *Tg(PiT1::EGFP-hATG7)* with *atg7* mutant zebrafish. For the rescue of LMW proteinuria, *atg7*$^{+/del4}$, *Tg(PiT1::EGFP-hATG7)* was crossed with *atg7*$^{+/del4}$, *Tg(lfabp::½vdbp-mCherry)* to produce double transgenic *atg7*$^{WT}$ and *atg7*$^{KO}$larvae. Overnight urine collection was performed at 10 and 14dpf for ELISA assay following the protocol described below.

**Swimming behaviour**. The movement tracking of zebrafish larvae was conducted using a custom-built setup, comprising a projector (HP vp6111) for background light, an infrared light source for camera-tracking, and a high-speed camera (Allied Vision Stingray) equipped with a Fujinon 1:1.4/12.5mm objective (Fujinon). Both tracking and background light control were executed through the open-source tracking software Stytra.[56] In each experiment, up to 10 larvae were situated in a specially designed arena featuring 10 lanes (1cm width x 16cm length), all filled with E3 medium. The tracking process involved monitoring larval swimming distances along each lane over 5 minutes. Larval identity was established by tracing a Region of Interest (ROI) on each lane, and the distance covered was calculated by summing the distances between each consecutive coordinate.

**Zebrafish urine collection and mCherry measurements.** Zebrafish larvae (AB background) were placed in a 48-well microplate with one larva/500 mL facility water/well and kept at 28°C for 16 hours, followed by urine collection for ELISA assay.[10,11] The levels of ½vdbp-mCherry were measured according to the manufacturer's protocol. Briefly, 50 μl of fish pool water containing urine was distributed to a 96-well microplate pre-coated with anti-mCherry antibody. A 50 μL mixture of capture antibody and detector antibody was added to each well and incubated at room temperature for 1 hour. The wells were rinsed three times with washing buffer and incubated with 100 μL of TMB development solution at room

temperature for 10 minutes. The reaction was stopped by adding 100μl of stop solution, followed by reading the absorbance of each well at 450 nm.

**Mouse models.** The mouse lines were used: *Atg7*$^{fl/fl}$ (ref. 16) and *γGt1*-Cre.[30] The *Atg7*$^{fl/fl}$ mice (C57BL/6J background) were obtained from the RIKEN repository (National BioResource Project, started by the Ministry for Education, Culture Sports, Science and Technology, Japan). The *Atg7*$^{fl/fl}$ mice were generated by inserting two Lox P sites around exon 14, which encodes the active site cysteine essential for activation of the conjugation substrates.[16] The Cre-expressing mouse line was obtained from The Jackson Laboratory (RRID: IMSR_JAX:012841). The rat proximal promoter to γ*Gt1* was used in a transgene construct to drive Cre recombinase expression.[30] The γ*Gt1-Cre* promoter becomes active around postpartum day 14, coinciding with the completion of nephrogenesis and thus targeting cortical tubular epithelium in mature kidneys.[30] The Cre-expressing mice (C57BL/6 x SJL background) were backcrossed (>10 times) into the C57BL/6 background. The PT-specific *Atg7*$^{KO}$ mice were generated by crossing mice carrying the respective LoxP-flanked alleles with *γGt1*-Cre transgenic mice. All mice were housed at the animal service centre of the University of Zurich under specific pathogen-free conditions and maintained under controlled temperature (22-25°C) and humidity (50-60%), with 12-h dark/light cycle and ad libitum access to tap water and standard chow (Diet AO3, SAFE). Kidneys were collected for analysis at the time of sacrifice. Both female and male mice at 4, 12, and 24 weeks of age were used for kidney function studies, whereas the other experiments were performed using mice at 12 and 24 weeks of age. Littermates not carrying the *γGt1-Cre* transgenes were used as controls in all experiments.

**Kidney function and metabolic parameters.** The mice were placed overnight in metabolic cages with ad libitum access to food and drinking water; urine was collected on ice, and body weight, water intake and diuresis were measured. Blood (from a sublingual vein) was

obtained after anaesthesia with ketamine/xylazine or isoflurane. Urine and blood parameters were estimated using UniCel DxC 800 proSynchron (Beckman Coulter, Fullerton, CA, USA). Urinary levels of low-molecular-weight CC16 were measured by using an ELISA according to the manufacturer's instructions (BIOMATIK EKU03200, Thermo Fischer Scientific, Waltham, MA). Albuminuria was measured via Coomassie Blue staining by using ProtoBlue Safe (National Diagnostics, EC-722, Atlanta, GA, USA) according to the manufacturer's instructions.

**Amino acid measurements in the urine**. Urinary amino acid concentrations were measured at the Functional Genomic Center Zurich, University of Zurich, using liquid chromatography-mass spectrometry (LC-MS/MS). Before injection, 50µL of urine was mixed with 10% sulfosalicylic acid, precipitated, and centrifuged for 10 minutes at 12000 rpm. The supernatant was then mixed with 30µL borate buffer, 5µL 500µM MSK-CAA-1 internal standard, and 10µL AQC solution, totalling 50µL. After a 10-minute incubation at 55°C, samples were loaded onto a Waters UPLC H-Class Plus system with an Acquity PLC Quadrupole Solvent Manager and Sample Manager. Derivatized amino acids were detected using a Waters Qda single quadrupole mass detector in positive mode with selected ion monitoring (SIR). The column was maintained at 55°C, and 1µL was injected. Gradient elution used 0.1% formic acid in water (eluent A) and in acetonitrile (eluent B) with a constant flow rate of 0.5 mL/min and the following gradient for solvent B: Initial: 1%, 0.0-1 min: 1%, 1-4 min: 13%, 4-8.5 min: 15%, 8.5-9.5 min: 95%, 9.5-11.5 min: 95%, 12-15 min: 1%. Data were analyzed using Masslynx 4.2 (Waters).

**Isolation of PT segments from mouse kidneys and primary cell cultures.** Kidneys were harvested from Atg7$^{PT\text{-}KO}$ mice and their control littermates or from *Atg5*$^{fl/fl}$, *Atg7*$^{fl/fl}$, and *Fip200*$^{fl/fl}$ mice. One kidney was split transversally; one half was fixed and processed for immunostaining, and the other half was flash-frozen, homogenized in 1mL of RIPA buffer with protease and phosphatase inhibitors, and processed for western blot analysis. The

contralateral kidney was used to generate primary cultures of mPTCs. Freshly microdissected PT segments were seeded onto collagen-coated chamber slides and/or collagen-coated 6- or 24-well plates and cultured at 37°C and 5% CO2 in DMEM/F12 with 0.5% dialyzed FBS, 15mM HEPES, 0.55mM sodium pyruvate, 0.1ml $L^{-1}$ non-essential amino acids, hydrocortisone, human EGF, epinephrine, insulin, triiodothyronine, TF, and gentamicin/amphotericin, pH 7.40, 325mOsm $kg^{-1}$. The medium was replaced every 48 hours. Confluent monolayers of mPTCs, expanded from the tubular fragments after 6-7 days, were characterized by a high endocytic uptake capacity and tested negative for mycoplasma contamination.

**Nutrient starvation protocols and cellular treatments.** The withdrawal of serum, glucose, and amino acids was achieved by washing mPTCs with Hank's balanced salt solution and placing them in either a normal growth or nutrient-deprived medium (amino acid-free RPMI) for the indicated times. Lysosomal proteolysis was inhibited, where indicated, by adding BafA1 (250 nM in cell culture medium for 2 or 4 hours). The cells were then processed and analysed as described below.

**Adenovirus transduction**. For expression studies, adenoviral constructs included a CMV control vector (Ad-CMV-GFP) and a vector carrying Cre-recombinase (Ad-Cre-GFP), both purchased from Vector Biolabs (University City Science Center, Philadelphia, USA). Adenovirus transduction was performed 24 hours after plating when the cells reached 70–80% confluence. Cells were incubated for 6 hours at 37°C with a culture medium containing the virus at a concentration of 30 x $10^5$ PFU/ml. Fresh culture medium was exchanged every 2 days, and the cells were cultured for 3 days (unless otherwise specified) before being collected for analysis.

**Proteomics**

*Sample preparation.* Cell pellets (~$5\times10^5$ cells; n = 4 mice/group) were lysed in 100 µL buffer, sonicated with HIFU (1 min, 85% amplitude), and boiled at 95°C for 10 min. Proteins were further extracted using a Tissue Lyser II (2 × 2 min at 30 Hz), boiled again for 10 min, and subjected to an additional 1-min HIFU. After centrifugation (20,000 × g, 10 min), protein concentration was measured with a Lunatic instrument. Fifty micrograms of protein per sample was digested by adding 10 µL "Digest" solution and incubating at 37°C for 60 min; digestion was stopped with 100 µL Stop solution. The mixture was filtered (3,800 × g), and peptides were washed, eluted, dried, and reconstituted in 40 µL of 3% acetonitrile/0.1% FA with 1 µL iRT peptides (1:100 dilution).

*Liquid chromatography-mass spectrometry analysis.* Peptides were analyzed on an Orbitrap Fusion Lumos (Thermo Scientific) with a Digital PicoView source (New Objective) and an M-Class UPLC (Waters). Solvent A was 0.1% FA; Solvent B was 0.1% FA in 99.9% acetonitrile. One microliter of peptides was loaded onto an MZ Symmetry C18 Trap Column (100 Å, 5 µm, 180 µm × 20 mm) and separated on a nanoEase MZ C18 HSS T3 Column (100 Å, 1.8 µm, 75 µm × 250 mm). The elution gradient was: 5% B for 3 min, 5–22% B over 80 min, 22–32% B over 10 min, then washed at 95% B for 10 min and re-equilibrated for 10 min. Samples were run in randomized order. The instrument acquired full-scan MS spectra (m/z 300–1,500) at 120,000 resolution (target 500,000 ions) and data-dependent MS/MS in the ion trap (quadrupole isolation at 0.8 Da, HCD at 35% energy, target 10,000 ions, max 50 ms injection time). Only precursors >5,000 intensity were selected (cycle time 3 s); charge states 1, unassigned, and >7 were excluded, with dynamic exclusion set to 20 s (10 ppm). Internal lock masses were m/z 371.1012 and 445.1200.

*Protein identification and label-free protein quantification.* Raw data were processed with MaxQuant (v1.6.2.3) using Andromeda against the SwissProt canonical mouse proteome (2019-07-09), its reversed decoy, and common contaminants. Fixed modification was carbamidomethylation (C); variable modifications were methionine oxidation and N-terminal acetylation. Trypsin/P was used, allowing peptides ≥7 amino acids with up to 2 missed

cleavages. FDR was set to 1% for peptides and 5% for proteins. Label-free quantification was enabled with a 2-minute match-between-runs window, and each file was processed separately for individual quantification. Protein fold changes were calculated from Intensity values in the proteinGroups.txt file, filtering for proteins with ≥2 peptides and ≤3 missing values. Data were normalized via a modified robust z-score, and p-values were computed using a pooled variance t-test. For proteins missing all measurements in one condition, a pseudo–fold change was calculated using the mean of the lowest 10% intensities. Finally, pathway analysis was performed with Network Analyst (http://www.networkanalyst.ca) on significantly changed proteins in mPTCs from Atg7 mouse kidneys.

**Metabolomics**

***Urine metabolite extraction and LC-MS analysis***

*Extraction.* Twenty microliters of creatinine-normalized urine were mixed with 80 µL of pre-cooled methanol. The mixture was incubated at –20°C for 1 h, then centrifuged at 10,000 rpm for 10 min at 4°C. The supernatant was transferred to a clean test tube, dried under a nitrogen stream, and reconstituted in an injection buffer (90% acetonitrile). Following a second vortex and centrifugation (10,000 rpm, 4°C, 10 min), the clear supernatant was transferred to Total Recovery Vials (Waters) for LC-MS injection. Method blanks, standard mixes, and pooled samples were prepared identically to serve as quality controls.

*LC-MS Data Acquisition.* Urine metabolites were separated using a Thermo Vanquish Horizon Binary Pump equipped with a Waters Premier BEH Amide column (150 mm × 2.1 mm). A gradient was applied using solvent A (10 mM ammonium bicarbonate in 5% acetonitrile, pH 9.0) and solvent B (10 mM ammonium bicarbonate in 95% acetonitrile), transitioning from 99% B to 30% B over 12 min. The injection volume was 3.5 µL, with a flow rate of 0.4 µL/min; the column was maintained at 40°C and the autosampler at 5°C. The LC was coupled via a HESI source to a Thermo Q Exactive mass spectrometer. MS1 and MS2 data were acquired in negative ion mode using Full MS/dd-MS² (Top5) over a mass range of 70–1050 m/z, at a resolution of 70,000 for MS1 and >17,500 for MS2. Quality controls were

performed using pooled samples, reference compound mixtures, and blanks to assess technical accuracy and stability.

*Untargeted Metabolomics Data Analysis*. Data were processed with Compound Discoverer (Thermo Scientific) in an untargeted workflow that included spectral selection, retention time alignment, compound detection and grouping, gap filling, background filtering, and constant median normalization. MS2-based identities were assigned by scoring fragmentation patterns against the mzCloud and mzVault databases. A filtering process then generated a manually annotated compound table, with features assigned the highest level of confidence based on the following criteria: signal-to-noise ratio > 3, mzCloud or mzVault match score > 50, mass error within ±5 ppm, match to an in-house MS1_RT library within ±10 sec, and acceptable chromatographic peak and MS2 spectral quality.

***Cellular metabolite extraction and LC-MS analysis***

*Sample Preparation.* Cellular metabolism was quenched by adding 80% pre-cooled methanol to the cells. After vortexing, samples were incubated at –20°C for 1.5 h. Proteins were precipitated by centrifuging at 10,000 rpm for 20 min at 4°C, and the clear supernatant was transferred to a new vial. The supernatant was then dried under a nitrogen stream and reconstituted in 20 µL water mixed with 80 µL injection buffer (90% acetonitrile, 8.8% methanol, 50 mM ammonium acetate, pH 7). Following another round of vortexing and centrifugation (10,000 rpm, 4°C, 10 min), the clear supernatant was transferred to Total Recovery Vials (Waters) for LC-MS injection. Method blanks, standard mixes, and pooled samples were prepared identically for quality control.

*LC-MS Data Acquisition.* Cell metabolites were separated using a Waters nanoAcquity UPLC with a BEH Amide capillary column (150µm × 50 mm, 1.7µm). A gradient was applied using solvent A (5 mM ammonium acetate in water) and solvent B (5 mM ammonium acetate in acetonitrile), transitioning from 5% A to 50% A over 12 min. The injection volume was 1 µL, with the flow rate adjusted from 3 to 2 µL/min. The UPLC was coupled to a Waters Synapt G2Si mass spectrometer via a nanoESI source. MS1 and MS2 data were acquired in

negative ion mode using MSE over a mass range of 50 to 1200 m/z at resolutions greater than 20,000.

*Untargeted Metabolomics Data Analysis.* Data were processed using Progenesis QI (Nonlinear Dynamics, Waters). Ion intensity maps were aligned to a reference dataset, and peak picking was performed on an aggregated map. Ions were identified by comparing accurate mass, adduct patterns, and isotope distributions with the Human Metabolome Database (HMDB) using a mass accuracy tolerance of 5 mDa; fragmentation patterns were also considered. All biological samples were analyzed in triplicate, with quality controls run on pooled samples and reference compound mixtures. Finally, pathway analysis of significantly altered metabolites in cells and urine samples was performed using MetaboAnalyst (http://www.metaboanalyst.ca) with default settings.

***Lipidomics***

*Extraction*: Lipid extraction was performed following a previously described method[57], with some modifications. A mixture of 1000 µL isopropanol: methanol (1:1) was added to each cell culture well. The plates were then incubated at -80 °C for 10 minutes. After incubation, the cells were scraped, and the resulting solution was transferred to Eppendorf tubes.
The samples were continuously mixed in a thermomixer (Eppendorf) at 25 °C (950 rpm) for 30 minutes. Protein precipitation was achieved by centrifugation at 16,000 g for 10 minutes at 25 °C. The resulting single-phase supernatant was collected, dried under nitrogen ($N_2$), and stored at -20 °C until further analysis. Before analysis, the dried lipids were reconstituted in 100 µL methanol: isopropanol (1:1).

*LC-MS analysis*: The lipidomics LC-MS method was performed as previously described, with some modifications[58-60]. A Waters Premier BEH C18 column (50 mm × 2.1 mm × 1.7 µm) was used at 60 °C for LC separation on a Thermo Vanquish Horizon tandem LC system. The injection volume was 2 µL in positive mode and 5 µL in negative mode, with a flow rate of 1 mL/min. A segmented gradient was applied, transitioning from 15% Buffer B to 99% Buffer B over a total gradient length of 7.5 minutes. The gradient segments were as follows: 0.0-1.0

min; 15-30%B,1.0-1.25 min; 30-48%B,1.25-5.0 min;48-82%B, 5.5-5.75; 82-99%B,5.75-6.0 min; isocratic at 99 %B,6.0-6.05; 99-15%B, 6.05-7.5; isocratic at 15%B.

For the MS method, a Thermo Exploris 480 instrument was used in data-dependent acquisition mode (DDA) with top 5. Heated electrospray ionization (HESI) was used in positive and negative polarities in separate runs (sheath gas = 30, auxiliary gas = 13, spray voltage = 3800 and -3500 V, in positive and negative modes respectively), vaporizer temperature= 350C and ion transfer tube temp = 300°C). Internal mass calibration was used at the start of each run, and mild trapping was set to true to minimize in-source fragmentation (after the ion funnel). MS1 settings were as follows: resolution, 60000, scan range (150-2000 m/z), AGC target (1e6), max. Injection time (10ms). MS2 scan settings were as follows: isolation window (1 m/z), the stepped normalized collision energy was set to 10, 30, and 340 NCE %, Resolution = 15000, max injection time (10msec), AGC target (1e5), RF lens = 50%.

*Data analysis*: Data analysis was performed using Thermo Compound Discoverer software (version 3.3). Lipid identification was conducted by matching spectra against the LipidBlast library, followed by visual inspection of mirror plots (library vs. data) to confirm spectral alignment and the presence of diagnostic fragments. Identification was validated according to the Lipid Standards Initiative guidelines, ensuring compliance with established fragmentation rules. Only lipids that met the criteria for expected fragmentation spectra, mass accuracy threshold, and retention time (RT) pattern were included in the analysis. Peak areas were normalized using median normalization, and statistical comparisons between groups were performed using a t-test after log transformation. Volcano plots and heatmaps were generated in R using the ggplot2 and ComplexHeatmap packages.

**RNA isolation, reverse transcription, and quantitative PCR.** Total RNA was extracted from mouse tissues or zebrafish larvae using the AurumTM Total RNA Fatty and Fibrous Tissue Kit (Bio-Rad, Hercules, CA). To eliminate genomic DNA contamination, DNAse I treatment was performed. Total RNA was then extracted with an RNAqueousR kit (Applied

Biosystems, Life Technologies). For cDNA synthesis, 1 µg of RNA was used with the iScript TM cDNA Synthesis Kit (Bio-Rad). Changes in mRNA levels of target genes were determined by relative RT-qPCR using a CFX96TM Real-Time PCR Detection System (Bio-Rad) and iQ TM SYBR Green Supermix (Bio-Rad). Analyses were performed in duplicate with 100nM of both sense and antisense primers in a final volume of 20 µL using iQTM SYBR Green Supermix (Bio-Rad). Specific primers were designed using Primer 3 (**Supplementary Tables 3 and 4**). PCR conditions were 95°C for 3 min, followed by 40 cycles of 15 sec at 95°C and 30 sec at 60°C. PCR products were sequenced with the BigDye terminator kit (Perkin Elmer Applied Biosystems) using the ABI3100 capillary sequencer (Perkin Elmer Applied Biosystems). Primer efficiency was determined by dilution curves. The program geNorm version 3.4 was used to assess the expression stability of candidate reference genes in kidneys, and six reference genes were selected to calculate the normalization factor. Relative changes in targeted gene expression compared to HPRT, GAPDH, β-actin, or eef1a1a mRNAs were calculated using the $2^{-\Delta\Delta Ct}$ formula.

**Endocytosis assays in mouse kidneys and cultured primary PT cells.**

**Mouse kidneys**. Receptor-mediated endocytosis and fluid-phase endocytosis were monitored in the PT segments of mouse kidneys by measuring the uptake of β-lactoglobulin (L3908, Sigma) and Alexa 647-conjugated dextran (D22914, Thermo Fisher Scientific), respectively. β-lactoglobulin was labelled with Cy5 using a TM2 Ab labelling kit (Amersham) according to the manufacturer's instructions. Fifteen minutes after tail-vein injection of Cy5-β-lactoglobulin (0.8 mg/kg BW) or Alexa 647-conjugated dextran (1.2 mg/kg BW), all mice were anaesthetized, and their kidneys were harvested and processed for confocal microscopy.

**Primary cells**. Endocytic uptake was monitored in mPTCs by incubating them for 60 minutes at 4°C with specific markers: 20µg/mL BSA-Alexa-Fluor-647 (A34785, Thermo Fisher Scientific), 40µg/mL Lysozyme-647 (provided by Dr. A. Hall, University of Zurich), or 20µg/mL Dextran-Alexa-Fluor-647 (Invitrogen, D22914) in complete HEPES-buffered

Dulbecco's modified Eagle's medium. After incubation, the cells underwent an acid wash and were warmed to 37°C in a growth medium for 15 minutes before fixation and processing for immunofluorescence analysis.

**Lysosomal degradation.** The detection of lysosomal activity was performed in mPTCs by using Bodipy-FL-Pepstatin A (P12271, Thermo Fischer Scientific) to the manufacturer's specifications. The cells were pulsed with 1μM Bodipy-FL-Pepstatin A in a Live Cell Imaging medium for 1h at 37°C, fixed and subsequently analyzed by confocal microscopy. The number of Pepstatin A - positive structures per cell was quantified by using the open-source cell image analysis software CellProfiler[61] as described below.

**Quantification of lipid droplet and pulse-chase experiments.** Cells were incubated in the dark for 30 min with 2 μM BODIPY 493/503 (D3922, Thermo Fisher Scientific) the staining solution prepared in a growth medium. The cells were washed 3 times in PBS, fixed in 4% PFA for 10 min, stained with DAPI for another 5 min, washed in PBS, and mounted in a drop of Prolong® Gold (P36934, Thermo Fisher Scientific). For pulse-chase experiments, palmitate (C16) was conjugated to BSA following the standard protocol from Seahorse Biosciences. BODIPY (D3821, Thermo Fisher Scientific) and PAL were conjugated in a 0.1% defatted bovine serum albumin solution for 30 min at 37°C. Cells were incubated with 0.5 μM BODIPY-PAL overnight and chased in a growth medium for 16 hours. The cells were washed 3 times in PBS, fixed in 4% PFA for 10 min, immunolabelled with a mitochondrial marker (TOMM20) and stained with DAPI, and analysed by confocal microscopy.

**Quantification of mitochondrial membrane potential and oxidative stress**. Mitochondrial membrane potential (Δψ) was assessed following the manufacturer's guidelines. Cells were treated with 50 nM Tetramethylrhodamine Methyl Ester Perchlorate (TMRM, T668, Thermo Fisher Scientific) and 1μM MitoTracker Red FM (Invitrogen, M22426) during a 30-minute live cell imaging session at 37°C. After washing, cells were analyzed using confocal microscopy

(Leica SP8, Center for Microscopy and Image Analysis, University of Zurich) within a chamber maintained at 37°C and 5% CO2. Fluorescence intensity was quantified using the open-source image processing software Fiji (ImageJ, NIH), as described below.

**Immunofluorescence and confocal microscopy**

*Mouse tissue slides***.** Fresh mouse kidneys were fixed by perfusion with 50-60 mL of 4% paraformaldehyde in PBS (158127, Sigma-Aldrich), followed by dehydration and embedding in paraffin at 58°C. Paraffin blocks were sectioned into consecutive 5 µm-thick slices using a Leica RM2255 rotary microtome (Thermo-Fisher Scientific) on Superfrost Plus glass slides (Thermo-Fisher Scientific). Before staining, slides were deparaffinized in Xylenes (534056, Sigma-Aldrich) and rehydrated. Antigen retrieval was performed by heating the slides at 95°C for 10 min in a 10 mM sodium citrate buffer (pH 6.0). Slides were then quenched with 50 mM NH4Cl, blocked with 3% BSA in PBS Ca/Mg (D1283, Sigma-Aldrich) for 30 min, and incubated with primary antibodies diluted in blocking buffer overnight at 4°C. After two washes in 0.1% Tween 20 (v/v in PBS), slides were incubated with fluorophore-conjugated Alexa secondary antibodies (Invitrogen) diluted in a blocking buffer at room temperature for 1 hour. They were subsequently counterstained with 1µg Biotinylated Lotus Tetragonolobus Lectin (LTL; B-1325, Vector Laboratories) and 1µM 4',6-Diamino-2-phenylindole dihydrochloride (DAPI; D1306, Thermo Fisher Scientific). Slides were mounted in Prolong Gold Anti-fade reagent (P36930, Thermo Fisher Scientific) and analyzed by confocal microscopy using a Leica SP8 confocal laser scanning microscope (Center for Microscopy and Image Analysis, University of Zurich).

*Primary cultured cells*. The cells were fixed for 10 minutes with 4% paraformaldehyde (PFA) in PBS, quenched with 50 mM NH4Cl, and permeabilized for 20 minutes in a blocking buffer solution containing 0.1% Triton X-100 and 0.5% BSA dissolved in PBS. Subsequently, cells were incubated overnight with the appropriate primary antibodies at 4°C. After repeated washing with PBS, the slides were incubated for 45 minutes with the suitable fluorophore-conjugated Alexa secondary antibodies (Invitrogen), counterstained with 1µM DAPI for 5

minutes, mounted with Prolong Gold Anti-fade reagent, and analyzed using a Leica SP8 confocal laser scanning microscope (Center for Microscopy and Image Analysis, University of Zurich).

*Image processing and quantification***.** Images were acquired with a Leica APO 63x NA 1.4 oil immersion objective at a resolution of 1,024 x 1,024 pixels (average of eight or sixteen scans), adjusting the pinhole diameter to 1 Airy unit for each emission channel to ensure intensity values between 1 and 254 (linear range). Micrographs were processed using Adobe Photoshop CS5 software (Adobe Systems Inc., San Jose, USA). Quantitative image analysis involved selecting randomly 5-10 visual fields per slide containing at least 3-5 proximal tubules (LTL-positive or AQP1-positive as indicated) or 10-15 cells. Setting parameters were consistently applied across analyses, including pinhole size, laser power, and offset gain, ensuring detector amplification remained below pixel saturation. Subcellular structure analyses were performed using the open-source software CellProfiler[61], specifically utilizing the "Measure-Object-Intensity-Distribution" module to quantify the number of Map1Lc3b- or Sqstm1- or BSA- or Lysozyme- positive structures. The “Cytoplasm-Nucleus Translocation Assay” was used to score the numbers of BrdU-positive nuclei. For measurements such as tubular height in mouse kidneys, mitochondrial morphology, and mitochondrial membrane potential, image analysis was carried out using Fiji v.2.0.0 (ImageJ, NIH). For the quantification of colocalization, non-overlapping images were acquired from each coverslip. Raw, unprocessed images were imported into FIJI v.2.0.0-rc-69/1.52i and converted to 8-bit images, and images of individual channels were thresholded independently to eliminate background and non-specific staining noise and converted to binary masks. Co-localization between Bodipy green-C16 and TOMM20 was determined using the “AND” function of the image calculator. The number of cells and/or fields of view used per condition and the number of biologically independent experiments are indicated in the figure legends.

*Imaging of zebrafish larvae*. Quantitative analysis of fluorescent signals involved examining an entire pronephric tubule from each zebrafish larva, maintaining consistent setting parameters throughout the process. A multi-photon fluorescence microscope (Leica SP8 MP

DIVE Falcon; Leica Microsystems, Heerbrugg, Switzerland) equipped with a 25/1.0 NA water immersion objective (HC IRAPO L, Leica) was used for capturing high-resolution images. The excitation wavelength was generated by a 1040 nm tunable laser for mCherry imaging. A light sheet fluorescence microscope (ZEISS Light sheet Z.1, Carl Zeiss Microscopy, Jena, Germany) equipped with a 20×/1.0 NA water immersion objective (W Plan APO, Zeiss) was used for detecting the human EGFP-ATG7 in mutant zebrafish larvae.

Data acquired underwent processing with Huygens software (Scientific Volume Imaging, Hilversum, The Netherlands) for deconvolution, followed by segmentation using Ilastik software (EMBL, Heidelberg, Germany). Quantitative analysis of fluorescence intensity, vesicle number, and vesicle area in each image stack was conducted using Fiji (ImageJ, NIH), an open-source image processing software. For the segmentation of Map1Lc3b spots, image stacks were analyzed using the object analyzer plugin within Huygens. This involved setting seed and threshold levels using algorithms, employing watershed segmentation, and filtering objects to isolate Map1Lc3b spots. A lower threshold was established to identify the entire kidney volume as a single object. The number of spots and extracted morphological parameters (such as length, volume, and sphericity) were exported in Excel format for subsequent statistical analysis. Surface images generated were used to create 3D volume-rendering images for visualization purposes.

**Immunohistochemistry**. Paraffin kidney sections were rehydrated, and antigen retrieval was performed either by heat-induced treatment in 10 mM sodium citrate buffer with 0.05% Tween-20 at pH 6.2 or by proteinase K treatment. Endogenous peroxidase activity was blocked using a peroxidase-blocking buffer for 15 minutes at room temperature. Sections were then blocked in a solution containing 1% BSA, 0.2% fish-skin gelatine, 0.2% Triton-X-100, and 0.05% Tween-20 in PBS for 1 hour at room temperature. Following blocking, sections were incubated overnight at 4 °C with a primary antibody against Cre (Cell Signaling 15036S, diluted 1:200). The next day, sections were incubated with biotinylated anti-mouse IgG (H+L) secondary antibody (Vector Laboratories, BA-9200- 1.5, diluted

1:1,000) or anti-Rabbit secondary antibody. Each staining was visualized using the ABC Kit Vectastain Elite (Vector, PK6100) and DAB substrate (Dako and Vector Laboratories).

**Histology and semiquantitative analysis of fibrosis.** Picrosirius red staining (ab150681, Abcam, Cambridge, UK) was performed following the manufacturer's instructions. Samples were rehydrated and incubated for 1 hour in picrosirius red solution. After incubation, samples were briefly rinsed in 0.5% acetic acid, dehydrated in absolute ethanol, cleared, and mounted. Evaluation of picrosirius red staining was conducted using a Zeiss AxioScanner.Z1 (Carl Zeiss, Oberkochen, Germany). Full scans of 24-week-old Atg7 kidneys were acquired at a resolution of 200× using a Zeiss Axio Scan.z1 slide scanner equipped with a Hitachi HV-F202FCL digital video camera (Hitachi, Tokyo, Japan). Images were captured and processed using ZENblue software (Carl Zeiss SpA).

**Electron microscopy**

*Primary cells*. Cultured mPTCs were fixed in 2.5% glutaraldehyde in 0.1 M cacodylate buffer (pH 7.4) at 37°C for 1 hour, followed by post-fixation in 1% osmium tetroxide and 1.5% potassium ferrocyanide in 0.1 M cacodylate on ice for 1 hour. After washing in distilled water, samples were stained with 0.5% uranyl acetate in water overnight at 4°C. Dehydration was performed in a graded ethanol series, followed by embedding in Epon 812 and curing at 60°C for 48 hours. Ultrathin sections (70–90nm) were cut using a Leica Ultracut UCT ultramicrotome, collected on copper grids, and stained with uranyl acetate and Sato's lead citrate. Imaging was conducted using a FEI Talos 120kV transmission electron microscope with a 4k×4K Ceta CMOS camera. Autophagic vacuoles (AVs) were identified and categorized as autophagosomes, or autolysosomes, based on established criteria.[17] At least 20 randomly selected cellular profiles were analyzed using ImageJ software to quantify AVs by calculating the percentage of cytosolic area occupied.

*Zebrafish larvae*. Animals were fixed in 2.5% glutaraldehyde and 1.6% paraformaldehyde in 0.1 M cacodylate buffer (pH 7.4) overnight after tail cutting. After rinsing in 0.1 M cacodylate

buffer, larvae were post-fixed in 1% osmium tetroxide in cacodylate buffer for 40 minutes at room temperature and stained with 1% aqueous uranyl acetate for 1 hour at room temperature. Samples were dehydrated through a graded ethanol series, infiltrated with Epon812 at 60°C for 28 hours, and then sectioned into 350 nm semi-thin sections using a Leica EM FCS ultramicrotome. Sections were stained with Toluidine blue solution. Ultra-thin sections of 60 nm were collected onto formvar-coated copper grids, stained with lead phosphate dilution in water, and examined using an electron microscope (Philips CM100) at 80kV.

**Sample preparation and immunoblotting.** Proteins from animal tissues or cultured mPTCs were extracted using a lysis buffer containing protease inhibitors (Roche) and phosphatase inhibitors (PhosSTOP, Sigma). The lysates were sonicated and centrifuged at 16,000 × g for 10 min at 4°C. After thawing on ice, protein concentrations were normalized (20 μg/lane), and samples were dissolved in Laemmli sample buffer and separated by SDS-PAGE under reducing conditions. Proteins were then transferred onto PVDF membranes, which were blocked with 5% non-fat milk (Bio-Rad Laboratories, 1706404), followed by overnight incubation at 4°C with primary antibodies. After washing, membranes were incubated with peroxidase-labelled secondary antibodies, and protein bands were visualized using enhanced chemiluminescence (Millipore, WBKLS0050) and imaged with a ChemiDoc MP imaging system (Bio-Rad Laboratories). Signal intensities were quantified by measuring the relative density of each band normalized to β-actin using ImageJ software.

**Extracellular flux analysis and metabolic measurements.** Oxygen consumption rate (OCR) in mPTCs was assessed using XFp Extracellular Flux Analyzers from Agilent Seahorse Biosciences. Cells were cultured in XF-Base Medium (non-buffered RPMI 1640 supplemented with 2 mM L-glutamine, 1 mM sodium pyruvate, and 10 mM glucose, pH 7.4). OCR was measured under basal conditions and after the sequential addition of specific inhibitors using the XFp Cell Mito Stress Test Kit (Agilent Seahorse Biosciences). The

inhibitors included 2μM Oligomycin (to inhibit ATP synthase), 0.5μM FCCP (to uncouple mitochondrial respiration), and 1μM Rotenone/Antimycin A (to inhibit complex I and III of the mitochondrial electron transport chain). All OCR measurements were normalized to cell numbers using the TC10TM automated cell counter from Bio-Rad. This method allows for the assessment of mitochondrial function and cellular respiration dynamics in mPTCs.

**Cell proliferation.** mPTCs were seeded in 24-well plates at a density of $2.0 \times 10^4$ cells per well. To assess the rate of proliferation, we used the Click-iT Plus EdU Alexa Fluor 488 Imaging Kit (C10637 Life Technologies). Cells were incubated with EdU solution for 16 h at 37 °C and processed following the manufacturer's instructions. DAPI (4′,6-diamino-2-phenylindole dihydrochloride) was used to counterstain nuclei. Analyses were performed by using the "Cytoplasm-Nucleus Translocation Assay" (CellProfiler[61]) to score the numbers of BrdU-positive nuclei.

**Analysis of TCGA gene expression and survival data on cell renal cell carcinoma samples.** The Genebass browser (https://app.genebass.org/) provided detailed coefficients and p-values from burden tests assessing the association between Chapter II neoplasms (labelled with ICD10 codes) and pLOF alleles in *ATG7*. The entire cohort for clear cell renal cell carcinoma (KIRC) was downloaded from TCGA (The Tissue Cancer Genome Atlas). It included transcriptomic (in FPKM) and clinical data from 537 patients. In the first step of filtering, data from patients with insufficient clinical data for survival analysis were removed. Additionally, data from patients who had multiple RNA-seq performed on the same sample from tumour tissue were excluded. 525 patients remained after filtering, and 72 had available data from adjacent normal tissue samples to the primary tumour (Normal Tissue).The total number of samples obtained amounts to 597 RNA-seq samples from 525 patients. The entire data analysis was performed locally with Python (v. 3.11.5) using Pandas (v. 2.2.3), Numpy (v. 1.24.3), and glob libraries. The division into tertiles was performed using Numpy, considering only gene expression of *ATG7* in Primary Tumour data. The normal tissue

samples were assigned to the tertile of the corresponding primary tumour. Survival analyses were performed considering only the 525 transcriptomic data from tumour tissues (Primary Tumour). These analyses were performed using the lifelines library (v. 0.30.0). Violin plots were generated using the Seaborn (v. 0.11.2) and Matplotlib (v. 3.7.2) libraries, considering the transcriptomic data from both the 72 normal tissue samples and the 525 primary tumour samples.

**Data Collection and Integration Using PandaOmics AI Platform.** The PandaOmics AI platform (Insilico Medicine, Hong Kong, China) is a cloud-based software tool that leverages artificial intelligence and bioinformatics to analyse multimodal omics and biomedical text data for the discovery of therapeutic targets and biomarkers.[62] This platform was utilized to integrate omics datasets from the Gene Expression Omnibus[63] and ArrayExpress[64], combining these with samples of clear cell renal cancer tissues and adjacent normal kidney samples. Gene expression data were uploaded to PandaOmics, normalized and pre-processed following the standard protocols provided by the platform.

**Differential expression and pathway enrichment analyses**. The ccRCC gene signature was derived through a PandaOmics meta-analysis, which incorporated data from seven comparisons across seven distinct transcriptomic datasets. Differential expression analysis was conducted in PandaOmics utilizing the limma R package, with each dataset processed following standard limma protocols. Gene-wise p-values were adjusted using the Benjamini-Hochberg correction method. PandaOmics calculated combined log-fold changes (LFC) across transcriptomics datasets using the 'Expression' feature. This feature calculates combined LFC values and Q-values across all datasets used for the analysis, employing min-max normalization for LFC values and Stouffer's method for p-value aggregation, followed by additional FDR correction. All differentially expressed genes (DEGs) were subsequently downloaded and used to construct the final gene expression signature. Pathway enrichment analysis was performed with the GSEApy package[65] prerank function

according to standard protocols. For the prerank protocol, each gene was ranked according to the value derived from the multiplication of LogFoldChange and -log10(p-value) obtained from differential expression analysis results. MSigDB and Reactome databases were selected as the gene set from the GSEApy internal library for signalling pathway enrichment analysis.

**Single-cell RNA sequencing analysis.** Single-cell RNA sequencing (scRNA-seq) data from 167,283 cells from multiple tumour regions, lymph nodes, normal kidneys, and peripheral blood of two immune checkpoint blockade (ICB)-naïve and four ICB-treated ccRCC patients were collected from the Krishna et al study.[48] Cell type annotations were derived from the original publication as well as normalized counts, and dimensionality reduction post-batch correction for the UMAP. Differential expression between ccRCC and control samples for each cell type was calculated using the tl.rank_genes_groups function (method='Wilcoxon'). ATG7 expression levels (non-zero values) were plotted with corresponding p-values (threshold: 0.05) using the Plotly package.

**Statistics and reproducibility.** The data were presented as mean ± SEM. Statistical analyses were conducted using appropriate tests: one-way analysis of variance (ANOVA) with Tukey's, Sidak's, or Dunnett's post hoc tests for multiple comparisons between experimental groups, as required. For comparisons between two groups, two-tailed unpaired or paired Student’s t-tests were used as appropriate. Normality was assessed using the D’Agostino and Pearson omnibus test. Non-parametric data were analysed using the Kruskal-Wallis test with Dunn's multiple comparison correction. Outliers were identified using the ROUT method (Q=1%). The sample size for each experimental group is detailed in the figure legends. Statistical significance levels are denoted by symbols, and the exact P-values are provided in the figure legends along with the specific statistical tests used. Each experiment was independently performed at least two to three times unless otherwise specified in the figure legends, and successful replication was achieved in all instances.

Experimenters were not blinded to allocation during most experiments, except for experiments involving zebrafish larvae. GraphPad Prism software version 9.4.1 (GraphPad Software) was used for all statistical analyses and figure generation.

## References


1. Palm, P. & Thompson, C.B. Nutrient acquisition strategies of mammalian cells. *Nature* **546**, 234-242 (2017).

2. Efeyan, A. *et al*. Nutrient-sensing mechanisms and pathways. *Nature* **517**, 302-315 (2015).

3. Keller, S. A. et al. Drug discovery and therapeutic perspectives for proximal tubulopathies. *Kidney Int.* **6**, 1103-1112 (2023).

4. van der Wijst, J. et al. Learning physiology from inherited kidney disorders. *Physiol Rev.* **99**, 1575-1663 (2019).

5. Nielsen, R., Christensen, E.I., Birn, H. Megalin and cubilin in proximal tubule protein reabsorption: from experimental models to human disease. *Kidney Int.* **89**, 58-67 (2016).

6. Cullen, P. J. & Steinberg, F. To degrade or not to degrade: mechanisms and significance of endocytic recycling. *Nat. Rev. Mol. Cell Biol.* **19**, 679-696 (2019).

7. Mizushima, N. & Levine, B. Autophagy in human diseases. *N. Engl. J. Med*. **381**, 1564-1576 (2020).

8. De Leo, M. G. et al. Autophagosome-lysosome fusion triggers a lysosomal response mediated by TLR9 and controlled by OCRL. *Nat. Cell Biol.* **18**, 839-850 (2016).

9. Luciani, A. et al. Impaired lysosomal function underlies monoclonal light chain-associated Renal Fanconi Syndrome. *J. Am. Soc. Nephrol*. **27**, 2049-2061 (2016).

10. Festa, B. P. et al. Impaired autophagy bridges lysosomal storage disease and epithelial dysfunction in the kidney. *Nat. Commun*. **9**, 161 (2018).

11. Berquez, M. et al. Lysosomal cystine export regulates mTORC1 signaling to guide kidney epithelial cell fate specialization. *Nat. Commun*. **14**, 3994 (2023).

12. Yamamoto, H. et al. Autophagy genes in biology and disease. *Nat. Rev. Genet*. **24**, 382-400 (2023).

13. Nakatogawa, H. Mechanisms governing autophagosome biogenesis. *Nat. Rev. Mol. Cell Biol.* **21**, 439-458 (2020).

14. Mizushima, N. et al. Dissection of autophagosome formation using Apg5-deficient mouse embryonic stem cells. *J. Cell Biol.* **152**, 657-668 (1998).

15. Ichimura, Y. et al. A ubiquitin-like system mediates protein lipidation. *Nature* **408**, 488-492 (2000).

16. Komatsu, M., Waguri, S., Ueno, T. et al. Impairment of starvation-induced and constitutive autophagy in Atg7-deficient mice. *J. Cell Biol.* **169**, 425-434 (2005).

17. Klionsky, D. J. et al. Guidelines for the use and interpretation of assays for monitoring autophagy (4th edition). *Autophagy* **17**, 1-382 (2021).

18. Collier, J. J. et al. Emerging roles of ATG7 in human health and disease. *EMBO Mol. Med.* **13**, e14824 (2021).

19. Komatsu, M. et al. Loss of autophagy in the central nervous system causes neurodegeneration in mice. *Nature* **441**, 880–884 (2006).

20. Kimura, T. et al. Autophagy protects the proximal tubule from degeneration and acute ischemic injury. *J. Am. Soc. Nephrol.* **22**, 902–913 (2011).

21. Liu, S. et al. Autophagy plays a critical role in kidney tubule maintenance, aging, and ischemia-reperfusion injury. *Autophagy* **8**, 826–837 (2012).

22. Wang, Z. M. et al. Specific metabolic rates of major organs and tissues across adulthood: evaluation by mechanistic model of resting energy expenditure. *Am. J. Clin. Nutr.* **92**: 1369–1377 (2010).

23. Hall, A.M. et al. Multiphoton imaging reveals differences in mitochondrial function between nephron segments. *J. Am. Soc. Nephrol.* **20**:p 1293-1302 (2009).

24. van der Rijt, S. et al. Immunometabolic rewiring of tubular epithelial cells in kidney disease. *Nat. Rev. Nephrol.* **18**, 588-603 (2022).

25. Bhargava, P. and Schnellman, R.G. Mitochondrial energetics in the kidney. *Nature Reviews Nephrology* **13**, 629-646 (2017).

26. Dijon, P. et al. The nuclear receptor ESRRA protects from kidney disease by coupling metabolism and differentiation. *Cell Metab.* **33**, 379-384 (2021).

27. Doke, T., Mukerjee, S., Mukhi, D. et al. NAD+ precursor supplementation prevents mtRNA/RIG-I-dependent inflammation during kidney injury. *Nature Metabolism* **5**, 414-430 (2023).

28. Emma, F., Montini, G., Parikh, S.M., Salviati, L. Mitochondrial dysfunction in inherited renal diseases and acute kidney injury. *Nature Reviews Nephrology* **12**, 267-280 (2016).

29. Collier, J. J. Et al. Developmental consequences of defective ATG7-mediated autophagy in humans. *N. Engl. J. Med.* **384**, 2406-2417 (2021).

30. Iwano, M. et al. Evidence that fibroblasts derive from epithelium during tissue fibrosis. *J. Clin. Invest*. **110**, 341-350 (2002).

31. Perez Bay, A. E. et al. The fast-recycling receptor Megalin defines the apical recycling pathway of epithelial cells. *Nat. Commun*. **7**, 11550 (2016).

32. Jo, Y. S. et al. Phosphorylation of the nuclear receptor corepressor 1 by protein kinase B switches its corepressor targets in the liver in mice. *Hepatology* **62**, 1606–1618 (2015).

33. Liu, G. Y. & Sabatini, D. M. mTOR at the nexus of nutrition, growth, ageing and disease. *Nat. Rev. Mol. Cell Biol.* **21**, 183-203 (2020).

34. Nguyen, T. B., et al. DGAT1-dependent lipid droplet biogenesis protects mitochondrial function during starvation-induced autophagy. *Developmental Cell* **42**: 9-21 (2017).

35. Singh, R. et al. Autophagy regulates lipid metabolism. *Nature* **458**, 1131–1135 (2009).

36. Weng Siong Tan, H. et al. A degradative to secretory autophagy switch mediates mitochondria clearance in the absence of the mATG8-conjugation machinery. *Nature Communications* **13**, 3720 (2022).

37. Cunha, L. D. et al. LC3-associated phagocytosis in myeloid cells promotes tumor immune tolerance. *Cell* **175**, 429–441 (2018).

38. Heckmann, B. L. et al. LC3-associated endocytosis facilitates beta-amyloid clearance and mitigates neurodegeneration in murine Alzheimer's disease. Cell 178, 536–551 (2019).

39. Kumar, A. V. et al. Lipid droplets modulate proteostasis, SQST-1/SQSTM1 dynamics, and lifespan in C. elegans. *iScience* **26**, 107960 (2023).

40. MacRoe, C. A. & Peterson, R. T. Zebrafish as tools for drug discovery. *Nat Rev Drug Discov*. **14**, 721–730 (2015).

41. Chen, Z. et al. Transgenic zebrafish modelling low-molecular-weight proteinuria and lysosomal storage diseases. *Kidney Int.* **97**, 1150-1163 (2020).

42. Verma et al. Diversity and scale: Genetic architecture of 2068 traits in the VA Million Veteran Program. *Science* **385**, 275 (2024).

43. Mizushima, N. & Levine, B. Autophagy in human diseases. *N. Engl. J. Med.* **383**, 1564–1576 (2020).

44. Pan, X. et al. Molecular subtyping and characterization of clear cell renal cell carcinoma by tumour differentiation trajectories. *iScience* **26**, 108370 (2023).

45. Tan, S. K. et al. Fatty acid metabolism reprogramming in ccRCC: mechanisms and potential targets. *Nature Reviews Urology* **20**, 48-59 (2023).

46. Karczewski, K. J., Solomonson, M., Chao, K. R., Goodrich, J. K., Tiao, G., et al. Systematic single-variant and gene-based association testing of thousands of phenotypes in 394,841 UK Biobank exomes. *Cell Genomics* **2**, 100168 (2022).

47. Tang, Z. et al. GEPIA2: an enhanced web server for large-scale expression profiling and interactive analysis. *Nucleic Acids Research* **47**, W556-560 (2019).

48. Krishna, C. et al. Single-cell sequencing links multiregional immune landscapes and tissue-resident T cells in ccRCC to tumour topology and therapy efficacy. *Cancer Cell* **39**, 662-677.e6 (2021).

49. Galluzzi, L. & Green, D. Autophagy-Independent Functions of the Autophagy Machinery. *Cell*. **17**, 1682-1699 (2019).

50. Mailler, E. et al. The autophagy protein ATG9A enables lipid mobilization from lipid droplets. *Nat. Commun.* **12**, 6750 (2021).

51. Yuan, Z. et al. ATG14 targets lipid droplets and acts as an autophagic receptor for syntaxin18-regulated lipid droplet turnover. *Nat. Commun.* **15**, 631 (2024).

52. Ganley, I. The Importance of Being Autophagic. *N. Engl. J. Med*. **384,** 2449-2450 (2021).

53. Na, H. et al. Identification of lipid droplet structure-like/resident proteins in Caenorhabditis elegans. *Biochim. Biophys. Acta* **1853**, 2481–2491 (2015).

54. Liu, Y. et al. Hydroxysteroid dehydrogenase family proteins on lipid droplets through bacteria, C. elegans, and mammals. *Biochim. Biophys. Acta Mol. Cell.* Biol. Lipids **1863**, 881–894, (2018).

55. Bae, S. et al. Cas-OFFinder: a fast and versatile algorithm that searches for potential off-target sites of Cas9 RNA-guided endonucleases. *Bioinformatics* **30**, 1473-1475 (2014).

56. Štih, V. et al. Stytra: An open-source, integrated system for stimulation, tracking and closed-loop behavioural experiments. *PLoS Comput. Biol.* **15**, e1006699 (2019).

57. Alshehry, Z. H., Barlow, C. K., Weir, J. M.; Zhou, Y., McConville, M. J., Meikle, P. J. An efficient single-phase method for extracting plasma lipids. *Metabolites.* **5**, 389–403 (2015).

58. Cajka, T., Fiehn, O. Increasing Lipidomic Coverage by Selecting Optimal Mobile-Phase Modifiers in LC–MS of Blood Plasma. *Metabolomics* **12**, 34 (2016).

59. Ganguin, A. A., Skorup I., Streb S., Othman A., Luciani P. Formation and Investigation of Cell-Derived Nanovesicles as Potential Therapeutics against Chronic Liver Disease. *Adv. Healthcare Mater.* **12**, 2300811 (2023).

60. Zareba, J., Cattaneo, E.F., Villani, A. et al. NPC1 links cholesterol trafficking to microglial morphology via the gastrosome. *Nature Communications* **15**, 8638 (2024).

61. Carpenter, A. E., Jones, T. R., Lamprecht, M. R. et al. CellProfiler: image analysis software for identifying and quantifying cell phenotypes. *Genome Biol.* **7**, R100 (2006).

62. Kamya, P. et al. PandaOmics: An AI-driven platform for therapeutic target and biomarker discovery. *J. Chem. Inf. Model.* **64**, 3961–3969 (2024).

63. Barrett, T. et al. NCBI GEO: archive for functional genomics data sets--update. *Nucleic Acids Res.* **41**, D991–5 (2013).

64. Parkinson, H. et al. ArrayExpress -- a public database of microarray experiments and gene expression profiles. *Nucleic Acids Res.* **35**, D747–50 (2007).

65. Fang, Z., Liu, X. & Peltz, G. GSEApy: a comprehensive package for performing gene set enrichment analysis in Python. *Bioinformatics* **39**, (2023).

**Acknowledgements**

We thank Nadine Nägele and Marco Garbelli for technical help, the Center for Microscopy, and Image Analysis at the University of Zurich for providing equipment and confocal microscopy assistance, and the Functional Genomics Center at the University of Zurich for assistance. We thank C.W. Li, P. Nanni, and S. Streb (Functional Genomics Center Zurich, University of Zurich) for their advice and constructive suggestions. We acknowledge Euro-Bioimaging (www.eurobioimaging.eu) for providing access to imaging technologies and services via the Italian Node (ALEMBIC, Milan, Italy). We are grateful to the Cystinosis Research Foundation [Irvine, CA, USA; project grants CRFS-2017-007 (O.D. and A.L.), CRFS-2020-005 (O.D. and A.L.) and CRFS 2022-003 (O.D.)], the Swiss National Science Foundation (project grant 310030_215715 to A.L.; and project grant 310030_204470 to C.M.), the University Research Priority Program of the University of Zurich (URPP) ITINERARE-Innovative Therapies in Rare Diseases (O.D. and A.L.). R.W.T. and R.M. are funded by the Wellcome Centre for Mitochondrial Research (203105/Z/16/Z), the Mitochondrial Disease Patient Cohort (UK) (G0800674), the Medical Research Council (MR/W019027/1), the Lily Foundation, the UK NIHR Biomedical Research Centre for Ageing and Age-related disease award to the Newcastle upon Tyne Foundation Hospitals NHS Trust and the UK NHS Highly Specialised Service for Rare Mitochondrial Disorders of Adults and Children. R.W.T. also receives additional funding from LifeArc and the Pathological Society. Postdoc Mobility-Stipendien of the Swiss National Science Foundation Grants P2ZHP3_195181 and P500PB_206851, Kidney Research UK Grant Paed_RP_001_20180925 supports EO.

**Authors contributions**

A.L. and O.D. conceived and supervised the study. D.N., S.K., O.D., and A.L. designed the experiments. D.N. and S.K. conducted immunoblotting analysis, RNA interference, gene expression experiments, confocal microscopy, live-cell imaging, molecular biology studies, and data analysis. Z.C. generated the *atg7* knockout zebrafish model and, together with D.N., performed complementation experiments in zebrafish larvae and data analysis. A.R. carried out electron microscopy studies and data analysis. V.B. performed deconvolution of MAP1BLC3-positive autophagosome structures in the zebrafish pronephros and analysed the data. M.B. and P.K. conducted differentiation and proliferation studies and data analysis. M.Z., M.R., and A.O. performed metabolomics- and lipidomics-based studies, and data analysis. R.M., R.W.T., A.M.S., E.G.O., and J.A.S. provided urine samples from two patients with loss-of-function *ATG7* variants and intellectual feedback. S.N. supervised D.N. in zebrafish swimming behaviour analysis. C.M. provided *Fip200* and *Atg5* floxed mouse lines and intellectual feedback. A.U. and M.K. analysed publicly available microarrays and bulk and single-cell RNA sequencing of ccRCC patient samples using artificial intelligence and data analysis. R.P., F.C., and E.R. performed genome-wide and phenome-wide association studies, gene expression, and survival analyses in ccRCC patients, along with statistical testing. A.M.O. carried out lipid droplet, autophagy, and bioenergetic studies in worms and performed data analysis. L.R.L. supervised A.M.O. and provided intellectual feedback. A.L. and O.D. drafted and edited the manuscript, incorporating input and comments from all authors.

**Competing interest**

A.U. and M.K. are affiliated with Insilico Medicine, a commercial company developing AI solutions for ageing research, drug discovery, and longevity medicine. The authors declare no competing interests.

## Figure legends

**Figure 1. Inactivation of ATG7 and autophagy in the PT segments of murine kidneys.** (**a**) Overview of the role of ATG7 in the canonical degradative autophagy. Signals that activate the autophagic process (initiation) typically originate from various conditions of stress. The Unc-51-like kinase 1 (ULK1) complex receives and integrates various upstream signals to execute the autophagic response. This response initiates the formation of a transient, double-membrane-bound structure known as a phagophore. The phagophore expands by incorporating ATG5–ATG12 conjugates and ATG8 proteins, such as LC3-II, ultimately maturing into an autophagosome. These components are produced through autophagy conjugation systems that rely on ATG7. In the subsequent stage, the mature autophagosome fuses with acidic compartments of the endolysosomal system, where resident hydrolytic enzymes degrade the engulfed cargo. (**b**) Diagram of the strategy for the generation of *Atg7* floxed alleles and mice with PT-specific (*Atg7*$^{fl/fl}$; *γGt1*$^{cre/cre}$) deletion of *ATG7*. (**c**) mRNA expression of the indicated genes in the kidney cortex of 12-week-old *Atg7*$^{PT\text{-}KO}$ (n=7) and CTR (n=8) mice. (**d-e**) Immunoblots and quantification of the indicated proteins in the kidney cortex samples of 12-week-old *Atg7*$^{PT\text{-}KO}$ and CTR mice; in **d**, n=4 animals and in **e**, n=3 animals per genotype. (**f,** left) Confocal microscopy and representative images of whole-kidney sections immunostained with antibodies against Umod (cyan) and Sqstm1 (red). The PT segments (green) and nuclei (grey) counterstained with Lotus tetragonolobus lectin (LTL; light blue) and 4′,6-diamidino-2-phenylindole (DAPI; grey), respectively. (**f**, right) Quantification of Sqstm1 fluorescence intensity, n=30 PT segments from 3 animals per genotype. Bar graphs show mean ± SEM. Statistics were calculated using unpaired two-tailed Student's *t*-test, **P<0.01, ***P<0.001 and $^{\#}$P< 0.0001 relative to CTR. Scale bar, 50μM.

**Figure 2. *Atg7*$^{PT\text{-}KO}$ mice display growth defects, metabolic dyshomeostasis and proximal tubulopathy.** (**a**) Schematic of the experimental workflow for measuring the phenotypic changes in CTR and *Atg7*$^{PT\text{-}KO}$ mice. At the indicated times, body weight, blood

and urine samples, and the kidneys were harvested and analysed. (**b**) Body weight of *Atg7*$^{PT\text{-}KO}$ and CTR mice at the age of 4, 12, and 24 weeks, n=20 animals per genotype. (**c**) Representative images of *Atg7*$^{PT\text{-}KO}$ and CTR mice at the age of 24 weeks. (**d**) Urinary excretion of the low-molecular-weight protein CC16 at the indicated times; n=19 CTR and n=20 *Atg7*$^{PT\text{-}KO}$ mice at 4 weeks, and n=20 mice per each genotype at the age of 12 and 24 weeks. (**e**) Coomassie blue-stained SDS-PAGE analysis of urine at 24 weeks of age and densitometry quantification of albumin; n = 8 mice per genotype). A total of 40 µg of BSA was loaded as a positive control (Mw ~ 66.5 kDa). (**f**) Representative immunoblots and quantification of the indicated proteins in the urine from 24-week-old *Atg7* mice, n=6 animals per genotype. (**g**-**h**) Measurements of (**g**) glucose and (**h**) phosphorus in the urine of 24-week-old *Atg7* mice. In **g**, n=17 *Atg7*$^{PT\text{-}KO}$ and n=15 CTR animals; in **h**, n=19 animals per genotype. (**i**) Measurements of amino acids in the urine of 24-week-old *Atg7* mice, n=5 animals per group. Ala, alanine; Arg, arginine; Asn, asparagine; Asp, aspartate; Cys, cysteine; Gln, glutamine; Glu, glutamate; Gly, glycine; His, histidine; Hyp, hydroxyproline; Ile, isoleucine; Leu, leucine; Lys, lysine; Met, methionine; Orn, ornithine; Phe, phenylalanine; Pro, proline; Ser, serine; Thr, threonine; Trp, tryptophan; Tyr, tyrosine; Val, valine. The urine parameters were normalized to urinary creatinine concentration. Bar graphs show mean ± SEM. Statistics were calculated using unpaired two-tailed Student's *t*-test, *P<0.05, **P<0.01, ***P<0.001, and #P< 0.0001 relative to CTR. NS, not significant.

**Figure 3. ATG7 loss diverts the differentiation of PT cells and their functioning states towards growth and proliferation.** (**a**) Schematic of the experimental workflow for the detection of receptor-mediated and fluid-phase endocytosis in the PT segments of *Atg7* murine kidneys. Twenty minutes after the tail vein injection of either Cy5-β-lactoglobulin (0.8 mg $kg^{-1}$) or Alexa 647-Dextran (1.2 mg $kg^{-1}$), the kidneys were fixed, processed, and analysed by confocal microscopy. (**b**) Confocal microscopy and quantification of Cy5-(red) or Alexa 647-Dextran (green) fluorescence intensities in the Aqp1$^{+}$ PT segments (grey) of *Atg7* murine kidneys; n=60 PT segments pooled from 2 mice per genotype. (**c**) mRNA expression

of the indicated genes in the kidney cortex of 24-week-old *Atg7*$^{PT-KO}$ and CTR mice, n=7 animals per genotype. (**d**) Confocal microscopy and quantification of Lrp2 fluorescence intensity in the LTL$^{+}$ PT segments of *Atg7* murine kidneys; n=100 PT segments pooled from 2 mice per genotype. (**e**) mRNA expression of the indicated genes in the kidney cortex of 24-week-old *Atg7*$^{PT-KO}$ and CTR mice, n=7 animals per genotype. (**f**) Confocal microscopy and quantification of the percentage of PCNA$^{+}$ (red) nuclei in the LTL$^{+}$ (green) PT segments of *Atg7* murine kidneys; n=90 PT segments pooled from 2 animals per genotype. Nuclei counterstained with DAPI (blue or grey). Bar graphs show mean ± SEM. Statistics were calculated using unpaired two-tailed Student's *t*-test, *P < 0.05, ***P<0.001, and $^{\#}$P<0.0001 relative to CTR. NS, not significant. Scale bars, 25μm in (**b**), (**d**), and (**f**).

**Figure 4**. **Dedifferentiation and proliferation in cultured PT cells lacking Atg7 and autophagy.** (**a**) Schematic of the experimental workflow for isolating and culturing primary cells derived from PT segments of *Atg7* murine kidneys. (**b, d**) Immunoblots (**b**) and quantification (**d**) of the indicated proteins in mPTCs from 24-week-old *Atg7* murine kidneys, n=3 biologically independent experiments. (**c, e-g**) mPTCs from *Atg7* murine kidneys were cultivated under fed or starved conditions, or starved conditions with the additional treatment of BafA1 (250 nM for 4 hours). (**c, e**) Immunoblots (**c**) and quantification (**e**) of the indicated proteins in mPTCs from 24-week-old *Atg7* murine kidneys, n=6 biologically independent experiments. (**f**) Confocal microscopy and quantification of the number of Map1lc3$^{+}$ structures. Fed conditions, n=1570 control cells and n=1413 *Atg7*$^{PT-KO}$ cells and starved conditions, n=910 CTR and n=1548 *Atg7*$^{PT-KO}$ cells pooled from 3 biologically independent experiments. Each dot represents the number of Map1Lc3b$^{+}$ structures in a cell. (**g**) Representative electron micrographs and quantification of cytoplasm area occupied by autophagy vacuoles or lysosome/multivesicular bodies (expressed as the percentage of the total area). AVs distribution, n=48 CTR and n=40 *Atg7*$^{PT-KO}$ cells pooled from 2 biologically independent experiments. Lysosomes/MVBs distribution, n=48 CTR and n=38 *Atg7*$^{PT-KO}$ cells pooled from 2 biologically independent experiments. Green and purple indicate EM-

compatible AVs or Lys/MVBs, respectively. (**h**) mRNA expression of the indicated PT cell-specific and proliferation genes in mPTCs from 24-week-old CTR and *Atg7*$^{PT-KO}$ mice, n=8 animals per genotype. (**i**) Confocal microscopy and quantification of BrdU$^{+}$ cells (expressed as a percentage of total cells); n=84 CTR and n=95 *Atg7*$^{PT-KO}$ cells randomly selected fields of views from 3 biologically independent experiments. (**j**) Confocal microscopy and quantification of BSA+ structures per cell; n=2096 CTR and n=1833 *Atg7*$^{PT-KO}$ cells from 3 biologically independent experiments. Each dot represents the number of BSA$^{+}$ structures in a cell. Nuclei counterstained with DAPI (blue or grey). Bar graphs show mean ± SEM. Statistics were calculated by unpaired two-tailed Student's t-test *P < 0.05, **P < 0.01, ***P < 0.001, $^{\#}$P < 0.0001 relative to fed CTR or starved CTR or starved *Atg7*$^{PT-KO}$. NS not significant. Scale bars, 25μm in (**f**), (**i**) and (**j**).

**Figure 5. Lipid droplet storage and altered mitochondrial bioenergetics in PT cells lacking ATG7.** (**a**) Kyoto Encyclopaedia of Genes and Genomes (KEGG) pathway analysis; n = 4 biologically independent experiments. The black dashed line shows the threshold of significant enrichment. Black circles show the size of enriched proteins and metabolites, respectively. P value was calculated from the enrichment analysis using Omicsnet2.0. (**b**) The cells were cultivated under fed or starved conditions and incubated with Bodipy 493/503, and fixed and analysed by confocal microscopy. Representative micrographs and quantification of the number of lipid droplets (yellow). Fed conditions, n = 1888 CTR and n = 1648 *Atg7*$^{PT-KO}$; and starved conditions, n = 1096 CTR and n = 856 *Atg7*$^{PT-KO}$ cells from 3 biologically independent experiments. Each dot represents the number of Bodipy$^{+}$ structures in a cell. Nuclei counterstained with DAPI (grey). (**c**) Heat-map of lipid changes in *Atg7*$^{PT-KO}$ mPTCs vs. CTR cells, n=4 biologically independent experiments. (**d**) Cells were pulsed with a fluorescent fatty acid analogue, Bodipy-C16 (green) for 16 hours. Following the pulse, cells were chased in a growth medium for an additional 16 hours to facilitate intracellular lipid trafficking. After the chase period, cells were fixed with 4% paraformaldehyde, permeabilized, and immunostained with an anti-TOMM20 antibody to visualize mitochondria.

(**e**) Representative confocal micrographs and quantification of Bodipy-C16/TOMM20$^{+}$ structures (expressed as a percentage of total mitochondria; n=15 randomly selected fields of view from 3 biologically independent animals). Dotted white squares contain images at high magnification. Nuclei counterstained with DAPI (grey). (**f**) Oxygen consumption rate (OCR) and individual parameters for basal respiration, ATP production and maximal respiration. OCRs were measured at baseline and after the sequential addition of Oligomycin (Oligo, 2μM), FCCP (2μM) and Rotenone (Rot; 1μM) + Antimycin A (Ant; 1μM); n = 9 replicates pooled from 3 biologically independent experiments. (**g** and **h**) Confocal microscopy and quantification of (**g**) TMRM and MitoSOX fluorescence intensity per cell; n = 20 cells from 2 biologically independent experiments. Representative images are shown in Supplementary Fig. 8. Bar graphs show mean ± SEM. Statistics were calculated by unpaired two-tailed Student's t-test *P < 0.05, **P < 0.01, ***P < 0.001, $^{\#}$P < 0.0001 relative to fed CTR or fed *Atg7*$^{PT\text{-}KO}$. Scale bars, 10 μm.

**Figure 6. Silencing of *Atg7* in PT cells alters mitochondrial energy metabolism, triggering dedifferentiation and dysfunction.** (**a**) Schematic of the experimental workflow for silencing *Atg7 in vitro*. mPTCs from *Atg7* floxed kidneys were transduced with adenovirus bearing Empty or Cre-recombinase for 3 days. (**b**) Immunoblots and quantification of the indicated proteins, n=3 biologically independent experiments. (**c-d**) Transduced cells were cultivated under fed or starved conditions, or starved conditions with the additional treatment of BafA1 (250 nM for 4 hours). (**c**) Immunoblots and quantification of the indicated proteins, n=5 biologically independent experiments. (**d**) Confocal microscopy and quantification of the number of Sqstm1$^{+}$ structures; Empty, n= 458 fed cells and n=398 starved cells and n=557 starved cells treated with BafA1, +Cre, n=349, n=404 starved, n=438 starved cells treated with BafA1 pooled from 2 biologically independent experiments. (**e**) The ratio between mitochondrial (*Nd1*) and nuclear DNA (*Gapdh*) was determined by quantitative PCR; Empty, n=8 and +Cre, n=7 biologically independent experiments. (**f**) The cells were loaded with MitoTracker (a fluorescent probe that localizes to mitochondria; 1μM for 30 min at 37 °C) and

analysed by confocal microscopy. Representative images and quantification of shape (expressed as circularity, left panel) or interconnectivity (right panel) of the mitochondrial network; each point representing the average values for circularity or interconnectivity in a cell, n=10 cells per each condition pooled from 2 biologically independent experiments. (**g**) Oxygen consumption rate (OCR) and individual parameters for basal respiration, ATP production and maximal respiration. OCRs were measured at baseline and after the sequential addition of Oligomycin (Oligo, 2μM), FCCP (2μM) and Rotenone (Rot; 1μM) + Antimycin A (Ant; 1μM); n=8 replicates pooled from 2 biologically independent experiments. (**h**) Confocal microscopy and quantification of $BrdU^+$ cells (expressed as a percentage of total cells); Empty, n=133 cells and +Cre, n=130 cells randomly selected fields of views from 3 biologically independent experiments. (**i** and **j**) mRNA expression of the indicated genes in *Atg7*$^{fl/fl}$ mPTCs, n=7 biologically independent experiments. (**k**) Confocal microscopy and quantification of BSA+ structures per cell; Empty, n = 466 cells and +Cre, n=387 cells pooled from 4 biologically independent experiments. Nuclei counterstained with DAPI (blue or grey). Plots show mean ± SEM. Statistics were calculated by unpaired two-tailed Student's *t*-test**,** *P<0.05, **P<0.01, ***P<0.001, #P<0.0001 relative to fed or starved cells transduced with Empty vector, or to starved cells transduced with Cre-recombinase. NS, not significant. Scale bars, 25μm in (**d**), (**h**) and (**k**).

**Figure 7. atg7 has a conserved role in C. elegans.** (**a**) Schematic of the experimental workflow for the detection of autophagy, lipid droplets, and oxygen consumption and respiration in nematodes. (**b**) Expression levels of autophagy receptor SQST-1::RFP fluorescence in WT and *atg7 (bp411)* mutant nematodes, n=10 animals per group. (**c**) Representative images and quantification of fluorescence intensity in the intestines of WT and *atg7 (bp411)* mutant nematodes expressing DHS-3::GFP, n=6 animals per group. (**d**) Analysis of oxygen consumption in WT and *atg7(bp411)* nematodes at day 4 adulthood (normalized by number of worms, n=4 biologically independent experiments). Bar graphs

show mean ± SEM. Statistics were calculated by unpaired two-tailed Student's t-test *P < 0.05, **P < 0.01, ***P < 0.001, #P < 0.0001 relative to WT nematodes.

**Figure 8. Loss of atg7-mediated autophagy impairs the function of pronephros in zebrafish.** (**a**) Kaplan-Meier survival curves of *atg7* zebrafish, n = 21 *atg7*$^{WT}$ and n = 17 *atg7*$^{KO}$ zebrafish larvae. (**b-c**) Swimming tracking (**b**) and quantification of distance (**c**) in *atg7* zebrafish larvae at the age of 5,10,14, and 19 dpf. Dots represent individual zebrafish larvae; n = 29 *atg7*$^{WT}$ and n = 27 *atg7*$^{KO}$ zebrafish larvae at 5dpf, n = 32 *atg7*$^{WT}$ and n = 20 *atg7*$^{KO}$ zebrafish larvae at 10dpf, n = 64 *atg7*$^{WT}$ and n = 21 *atg7*$^{KO}$ zebrafish larvae at 14dpf, n = 52 *atg7*$^{WT}$ and n = 24 *atg7*$^{KO}$ zebrafish larvae at 19dpf. (**d**) Experimental workflow for the detection of autophagy activity in *atg7* zebrafish line stably expressing a bona fide biosensor for autophagosome formation in the pronephros (*PiT::mCherry-MAP1LC3b*). (**e**) Multiphoton microscopy and quantification of the number of MAP1LC3B$^{+}$ structures in the pronephros of 5dpf-zebrafish larvae lacking *atg7*, n = 7 zebrafish larvae per genotype. (**f**) Experimental workflow for the generation of *atg7* transgenic zebrafish line stably expressing a bona fide biosensor for LMW proteinuria/PT function. The fate of ½vdbp-mCherry under normal conditions: ½vdbp-mCherry (~50 kDa) is (1) produced in the liver, (2) secreted into the bloodstream and filtered by the glomerulus, (3) reabsorbed by PT cells through receptor-mediated endocytosis, and (4) processed by the lysosome. EE, early endosome; LE, late endosome; Lys, lysosome. (**g-h**) The urine samples were harvested and analysed at the indicated times. (**g**) Quantification of urinary mCherry levels in *atg7* zebrafish larvae by ELISA; n = 19 *atg7*$^{WT}$ and n = 20 *atg7*$^{KO}$ zebrafish larvae at 10dpf; and n=19 zebrafish larvae at 14dpf. (**h**) Quantification of urinary mCherry levels in 14-dpf *atg7* zebrafish larvae stably expressing *ATG7* in the pronephros (*Pit1::GFP-hATG7*); n = 20 *atg7*$^{WT}$, n = 19 *atg7*$^{WT}$ + *hATG7*, n = 19 *atg7*$^{KO}$, and n=16 *atg7*$^{KO}$ + h*ATG7* zebrafish larvae. (**i** and **j**) Zebrafish larvae were treated with non-toxic doses of Etomoxir (1000 nM for 9 days). (**i**) Swimming behaviour tracking, n= 46 WT and n=47 *atg7*$^{KO}$ zebrafish larvae. (**j**) Quantification of urinary mCherry levels in 14-dpf *atg7* zebrafish larvae, n=16 animals per group. Dots represent individual

zebrafish larvae and bar graphs show mean ± SEM. Statistics were calculated using unpaired two-tailed Student's *t*-test, **P<0.01 and #P< 0.0001 relative to *atg7*$^{WT}$ or *atg7*$^{KO}$. NS, not significant. Scale bar, 200μM.

**Figure 9. Association of *ATG7* variants with kidney disease risk.** (**a**) View of the top-ranked trait/disease associations with *ATG7* locus. (**b**) Phenome-wide (PheWAS) for variant rs375156407, showing phenome-significant association with traits from the Million Veterans Program (MVP) biobank related to nephritis and nephropathy traits. Traits are sorted and coloured according to a meaningful set of biological categories. The direction of effect of the alternative allele's association with each trait is exhibited by upward-facing (positive effect) or downward-facing (negative effect) triangles. (**c**) Immunoblots of the low-molecular-weight protein CC16 in the urine samples of controls (n=6) and individuals with deleterious *ATG7* variants (n=2). (**d**) Schematic of the experimental workflow for metabolomics-based profiling of baseline and 1-follow-up urine samples from individuals with deleterious *ATG7* variants and pathway enrichment analysis. (**e**) Metabolite profiling and pathway enrichment analysis. The Black dashed line shows the threshold of significant enrichment. Black circles show the size of enriched proteins and metabolites, respectively. *P* value was calculated from the enrichment analysis using Omicsnet2.0.

**Figure 10. Changes in *ATG7* levels, differentiation and metabolic pathways correlate with reduced overall survival in patients with ccRCC. (a)** *ATG7* expression in healthy and tumour tissues in low vs medium/high *ATG7* expression tertiles. The *ATG7* expression levels in normal solid tissue (orange) and primary tumour tissue (teal) of individuals in the low-expression tertile (left), and in individuals in medium/high-expression tertiles (right). p-values calculated by the Wilcoxon test. Each point in the graph is *ATG7* FPKM of individual samples. (**b**) Survival of individuals with KIRC, stratified on *ATG7* expression. Kaplan-Meier survival curves of individuals with low expression of *ATG7* in the primary tumour (low-expression tertile, blue curve) against individuals with medium/high expression of *ATG7*

primary tumour (medium/high-expression tertiles – red curve). Significance was calculated with the log-rank test. (**c**) ccRCC human transcriptomic data analysis pipeline. The most complete publicly available transcriptomic data for ccRCC were collected. Data were integrated into PandaOmics, and combined meta-analysis was used for gene expression and MSigDB and Reactome pathway enrichment analyses. (**d**) Heat maps showing mRNA expression of *ATG7*, PT-specific, and proliferation/dedifferentiation genes in ccRCC tumour tissue compared to adjacent normal tissues. Differential expression analysis was performed in PandaOmics. The combined LFC across transcriptomic datasets was computed using PandaOmics via its 'Expression' analysis feature. (**e**) Heatmap and UMAPs showing mRNA expression of *ATG7* in different cell populations in untreated ccRCC patients' tumours compared to adjacent normal kidney samples (Wilcoxon, p-value < 0.05).

Figure 1

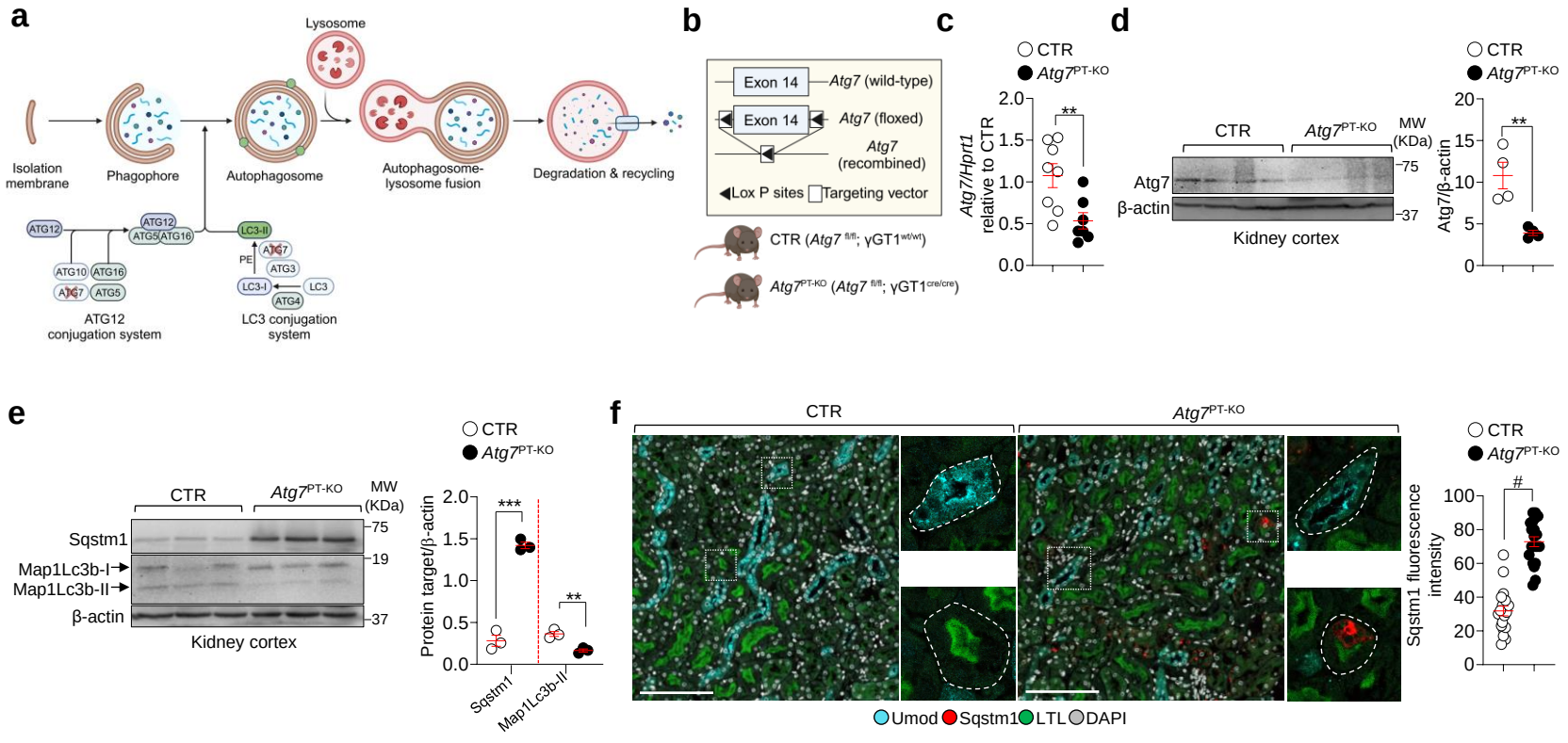
a
Lysosome
Isolation membrane
Phagophore
Autophagosome
Autophagosome-lysosome fusion
Degradation & recycling
ATG12
ATG12
ATG5
ATG16
ATG10
ATG16
ATG7
ATG5
ATG12 conjugation system
LC3-II
PE
ATG7
ATG3
LC3-I
LC3
ATG4
LC3 conjugation system
b
Exon 14
Atg7 (wild-type)
Exon 14
Atg7 (floxed)
Atg7 (recombined)
Lox P sites
Targeting vector
CTR (Atg7 fl/fl; γGT1 wt/wt)
Atg7PT-KO (Atg7 fl/fl; γGT1 cre/cre)
c
CTR
Atg7PT-KO
Atg7/Hprt1 relative to CTR
2.0
1.5
1.0
0.5
0.0
**
d
CTR
Atg7PT-KO
MW (KDa)
Atg7
β-actin
75
37
Kidney cortex
Atg7/β-actin
20
15
10
5
0
**
e
CTR
Atg7PT-KO
MW (KDa)
Sqstm1
Map1Lc3b-I
Map1Lc3b-II
β-actin
75
19
37
Kidney cortex
Protein target/β-actin
2.0
1.5
1.0
0.5
0.0
***
**
Sqstm1
Map1Lc3b-II
f
CTR
Atg7PT-KO
Sqstm1 fluorescence intensity
100
80
60
40
20
0
#
Umod
Sqstm1
LTL
DAPI

Figure 2

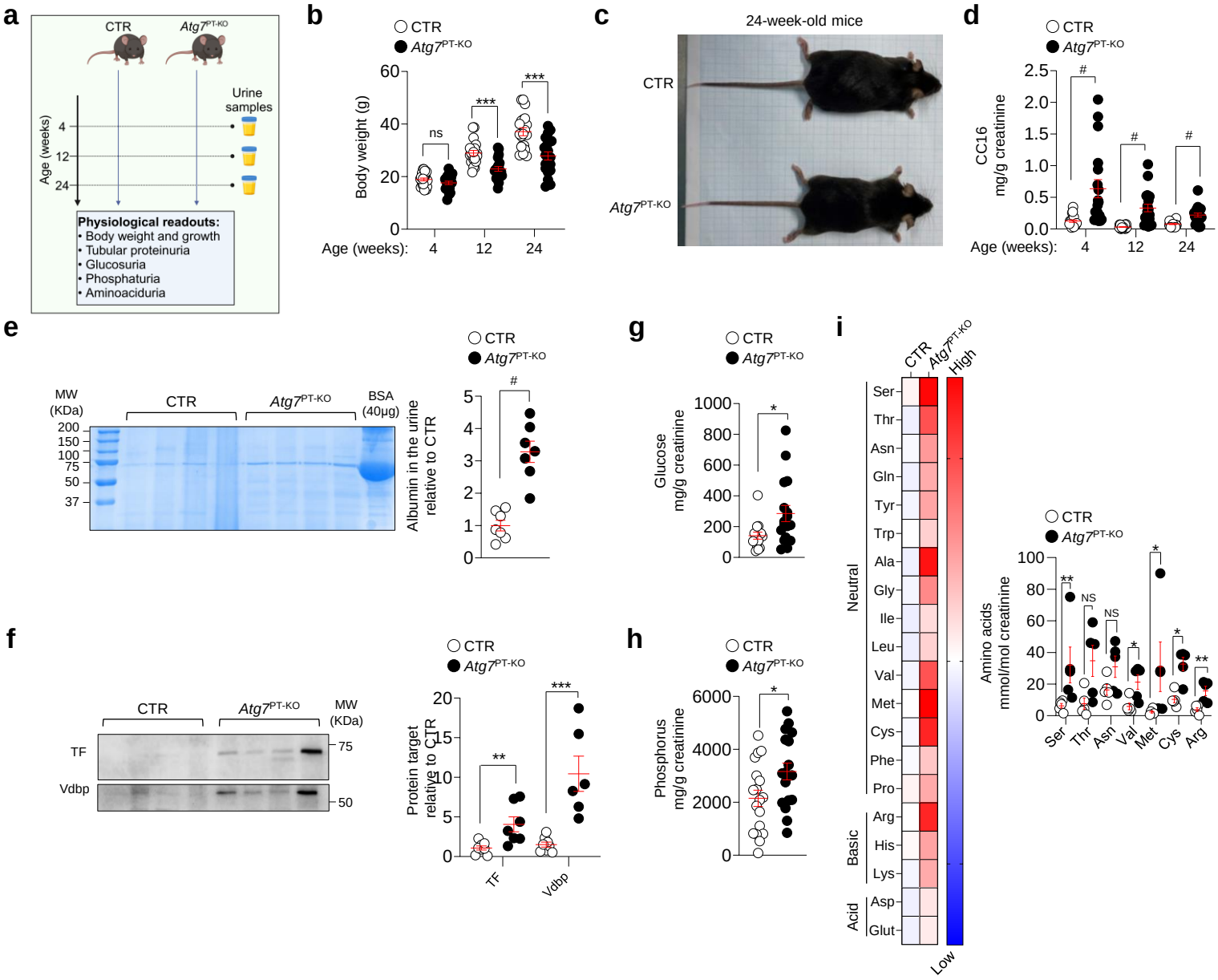
a
CTR
Atg7PT-KO
Urine samples
Age (weeks)
4
12
24
Physiological readouts:
• Body weight and growth
• Tubular proteinuria
• Glucosuria
• Phosphaturia
• Aminoaciduria
b
CTR
Atg7PT-KO
Body weight (g)
ns
***
***
Age (weeks): 4 12 24
c
24-week-old mice
CTR
Atg7PT-KO
d
CTR
Atg7PT-KO
CC16 mg/g creatinine
#
#
#
Age (weeks): 4 12 24
e
MW (KDa)
CTR
Atg7PT-KO
BSA (40µg)
200
150
100
75
50
37
CTR
Atg7PT-KO
Albumin in the urine relative to CTR
#
g
CTR
Atg7PT-KO
Glucose mg/g creatinine
*
f
CTR
Atg7PT-KO
MW (KDa)
TF
Vdbp
75
50
CTR
Atg7PT-KO
Protein target relative to CTR
**
***
TF
Vdbp
h
CTR
Atg7PT-KO
Phosphorus mg/g creatinine
*
i
CTR
Atg7PT-KO
High
Low
Neutral
Basic
Acid
Ser
Thr
Asn
Gln
Tyr
Trp
Ala
Gly
Ile
Leu
Val
Met
Cys
Phe
Pro
Arg
His
Lys
Asp
Glut
CTR
Atg7PT-KO
Amino acids mmol/mol creatinine
**
NS
NS
*
*
*
**
Ser
Thr
Asn
Val
Met
Cys
Arg

Figure 3

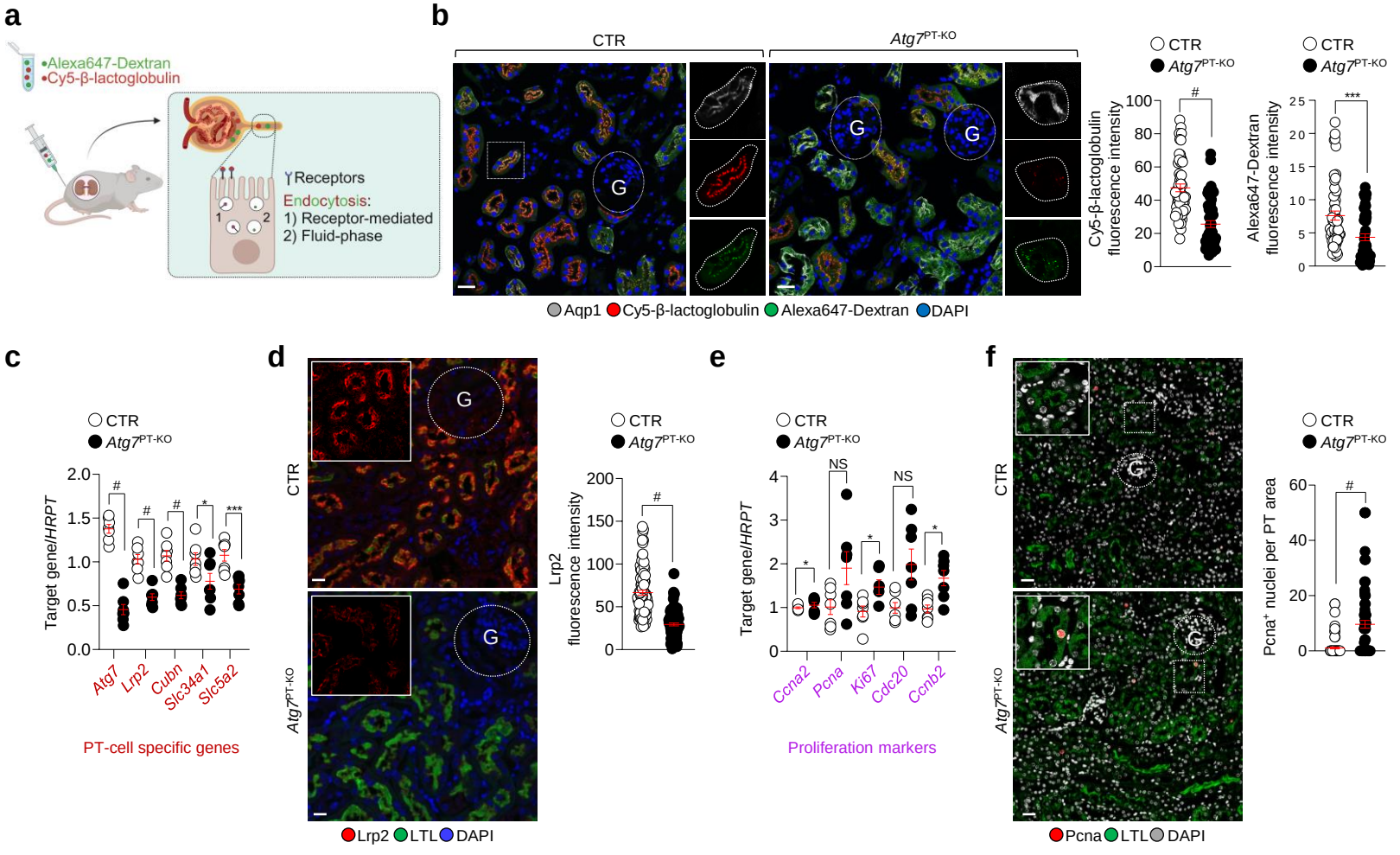
a
•Alexa647-Dextran
•Cy5-β-lactoglobulin
Receptors
Endocytosis:
1) Receptor-mediated
2) Fluid-phase
b
CTR
Atg7PT-KO
G
Aqp1 Cy5-β-lactoglobulin Alexa647-Dextran DAPI
Cy5-β-lactoglobulin fluorescence intensity
Alexa647-Dextran fluorescence intensity
c
Target gene/HRPT
Atg7
Lrp2
Cubn
Slc34a1
Slc5a2
PT-cell specific genes
d
Lrp2 fluorescence intensity
Lrp2 LTL DAPI
e
Ccna2
Pcna
Ki67
Cdc20
Ccnb2
NS
Proliferation markers
f
Pcna+ nuclei per PT area
Pcna LTL DAPI

Figure 4

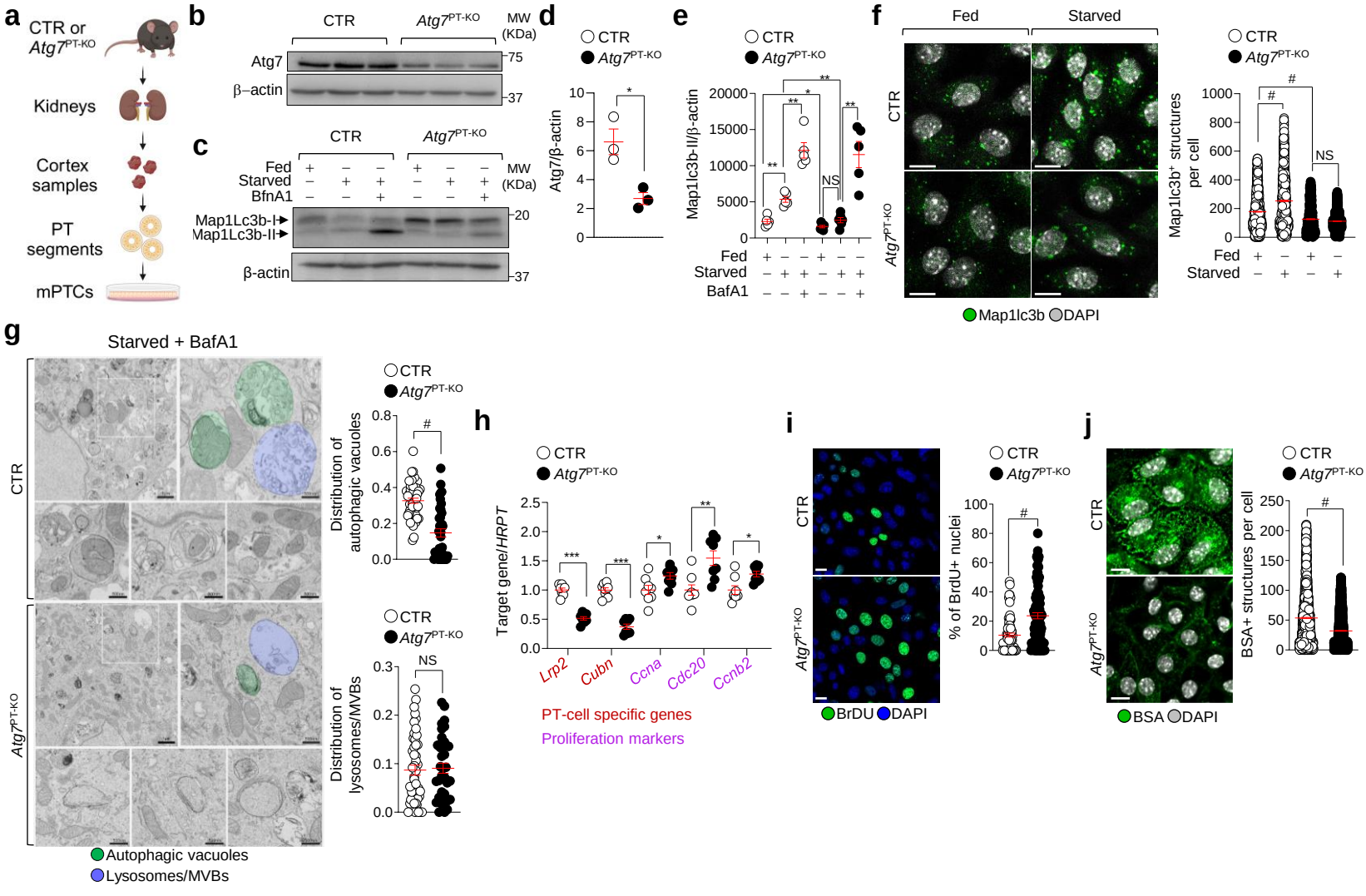
a
CTR or Atg7PT-KO
Kidneys
Cortex samples
PT segments
mPTCs
b
CTR
Atg7PT-KO
MW (KDa)
Atg7
β–actin
75
37
c
CTR
Atg7PT-KO
Fed
Starved
BfnA1
MW (KDa)
Map1Lc3b-I
Map1Lc3b-II
β-actin
20
37
d
CTR
Atg7PT-KO
Atg7/β-actin
e
CTR
Atg7PT-KO
Map1lc3b-II/β-actin
Fed
Starved
BafA1
NS
f
Fed
Starved
CTR
Atg7PT-KO
Map1lc3b DAPI
Map1lc3b+ structures per cell
NS
g
Starved + BafA1
CTR
Atg7PT-KO
Autophagic vacuoles
Lysosomes/MVBs
Distribution of autophagic vacuoles
Distribution of lysosomes/MVBs
NS
h
CTR
Atg7PT-KO
Target gene/HRPT
Lrp2
Cubn
Ccna
Cdc20
Ccnb2
PT-cell specific genes
Proliferation markers
i
CTR
Atg7PT-KO
BrDU DAPI
% of BrdU+ nuclei
j
CTR
Atg7PT-KO
BSA DAPI
BSA+ structures per cell

Figure 5

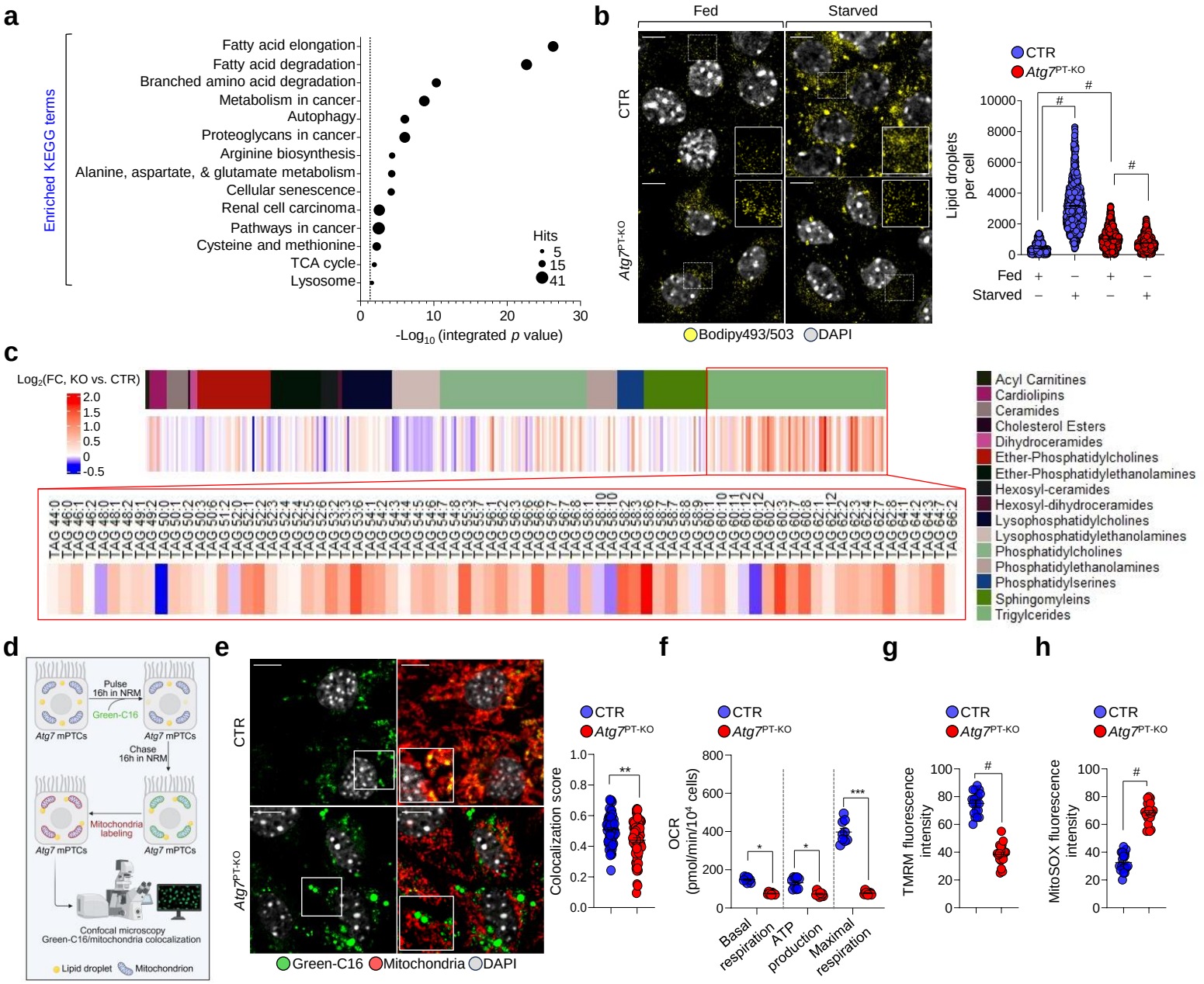
a
Enriched KEGG terms
Fatty acid elongation
Fatty acid degradation
Branched amino acid degradation
Metabolism in cancer
Autophagy
Proteoglycans in cancer
Arginine biosynthesis
Alanine, aspartate, & glutamate metabolism
Cellular senescence
Renal cell carcinoma
Pathways in cancer
Cysteine and methionine
TCA cycle
Lysosome
Hits
5
15
41
0
10
20
30
-Log10 (integrated p value)
b
Fed
Starved
CTR
Atg7PT-KO
Bodipy493/503
DAPI
CTR
Atg7PT-KO
Lipid droplets per cell
10000
8000
6000
4000
2000
0
#
#
#
Fed + − + −
Starved − + − +
c
Log2(FC, KO vs. CTR)
2.0
1.5
1.0
0.5
0
-0.5
Acyl Carnitines
Cardiolipins
Ceramides
Cholesterol Esters
Dihydroceramides
Ether-Phosphatidylcholines
Ether-Phosphatidylethanolamines
Hexosyl-ceramides
Hexosyl-dihydroceramides
Lysophosphatidylcholines
Lysophosphatidylethanolamines
Phosphatidylcholines
Phosphatidylethanolamines
Phosphatidylserines
Sphingomyleins
Trigylcerides
d
Pulse 16h in NRM
Green-C16
Atg7 mPTCs
Atg7 mPTCs
Chase 16h in NRM
Mitochondria labeling
Atg7 mPTCs
Atg7 mPTCs
Confocal microscopy
Green-C16/mitochondria colocalization
Lipid droplet
Mitochondrion
e
CTR
Atg7PT-KO
Green-C16
Mitochondria
DAPI
Colocalization score
1.0
0.8
0.6
0.4
0.2
0.0
**
f
CTR
Atg7PT-KO
OCR (pmol/min/10^4 cells)
800
600
400
200
0
*
*
***
Basal respiration
ATP production
Maximal respiration
g
CTR
Atg7PT-KO
TMRM fluorescence intensity
100
80
60
40
20
0
#
h
CTR
Atg7PT-KO
MitoSOX fluorescence intensity
100
80
60
40
20
0
#

Figure 6

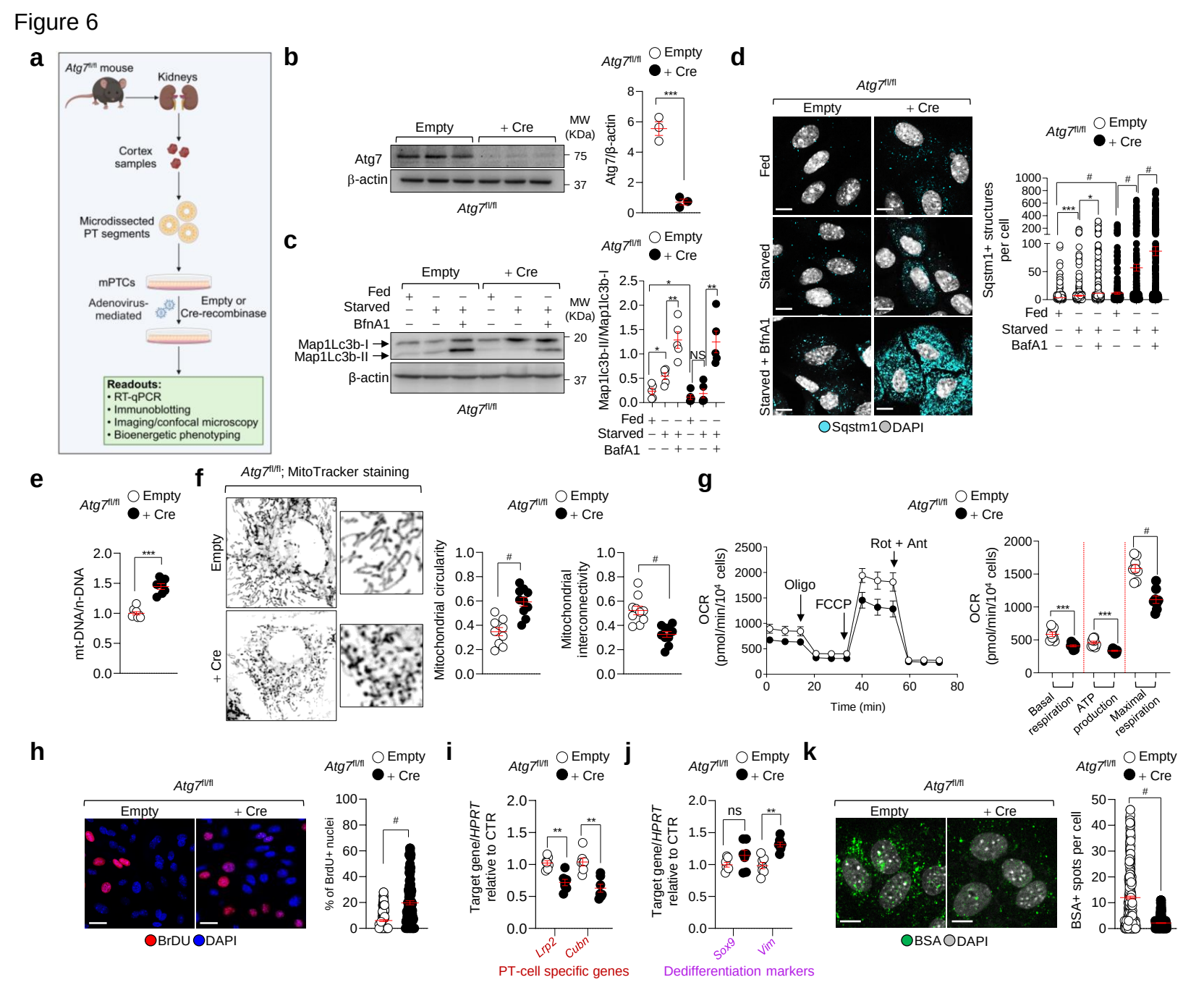
a
Atg7fl/fl mouse
Kidneys
Cortex samples
Microdissected PT segments
mPTCs
Adenovirus-mediated
Empty or Cre-recombinase
Readouts:
• RT-qPCR
• Immunoblotting
• Imaging/confocal microscopy
• Bioenergetic phenotyping
b
Empty
+ Cre
MW (KDa)
Atg7
β-actin
75
37
Atg7fl/fl
Atg7/β-actin
c
Fed
Starved
BfnA1
Map1Lc3b-I
Map1Lc3b-II
20
Map1lc3b-II/Map1lc3b-I
NS
BafA1
d
Sqstm1
DAPI
Sqstm1+ structures per cell
e
mt-DNA/n-DNA
f
Atg7fl/fl; MitoTracker staining
Mitochondrial circularity
Mitochondrial interconnectivity
g
OCR (pmol/min/10⁴ cells)
Oligo
FCCP
Rot + Ant
Time (min)
Basal respiration
ATP production
Maximal respiration
h
BrDU
% of BrdU+ nuclei
i
Target gene/HPRT relative to CTR
Lrp2
Cubn
PT-cell specific genes
j
ns
Sox9
Vim
Dedifferentiation markers
k
BSA
BSA+ spots per cell

Figure 7

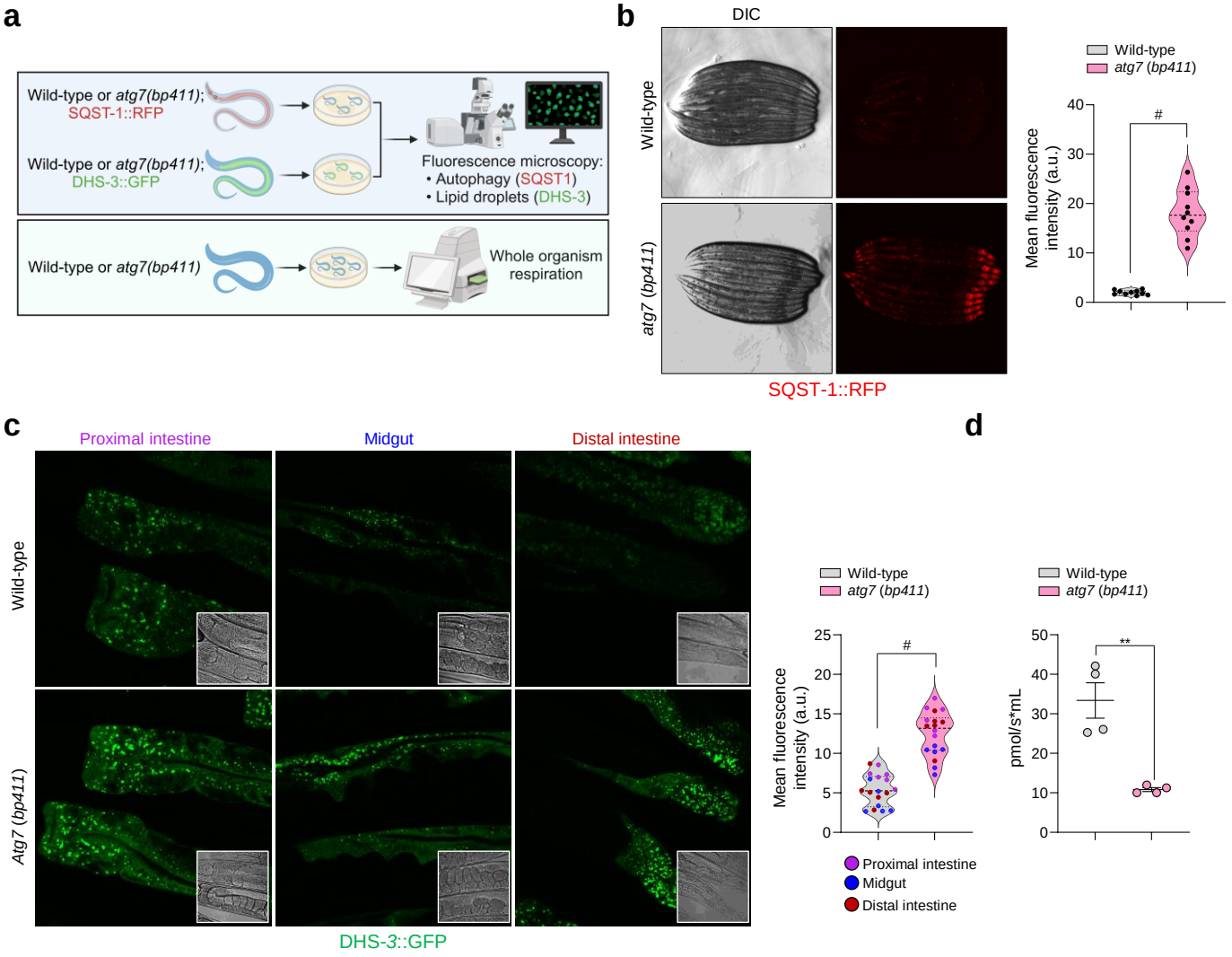
a
Wild-type or atg7(bp411);
SQST-1::RFP
Wild-type or atg7(bp411);
DHS-3::GFP
Fluorescence microscopy:
• Autophagy (SQST1)
• Lipid droplets (DHS-3)
Wild-type or atg7(bp411)
Whole organism respiration
b
DIC
Wild-type
atg7 (bp411)
SQST-1::RFP
Wild-type
atg7 (bp411)
Mean fluorescence intensity (a.u.)
#
c
Proximal intestine
Midgut
Distal intestine
Wild-type
Atg7 (bp411)
DHS-3::GFP
d
Wild-type
atg7 (bp411)
Mean fluorescence intensity (a.u.)
#
Proximal intestine
Midgut
Distal intestine
pmol/s*mL
**

Figure 8

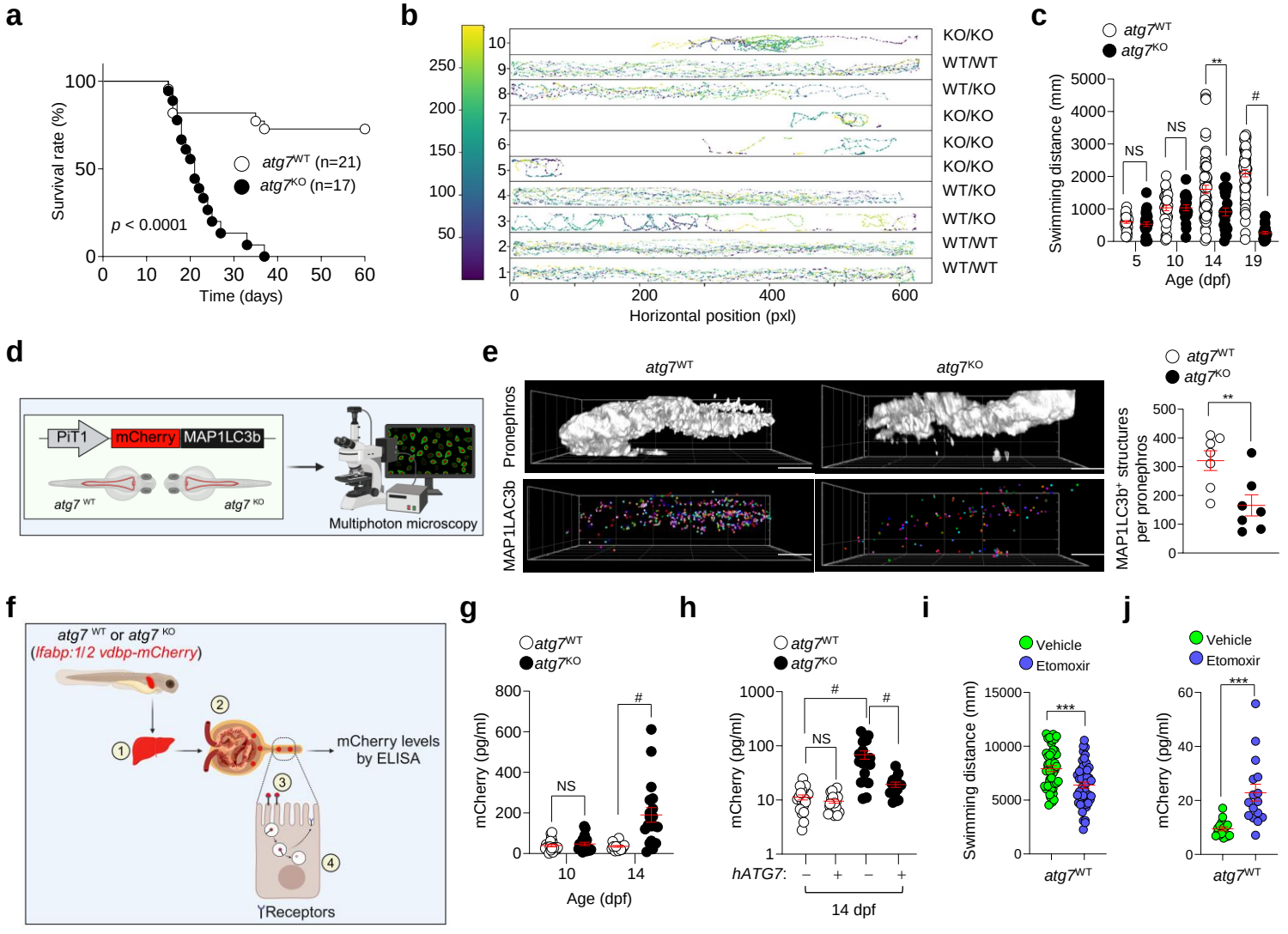
a
Survival rate (%)
Time (days)
atg7WT (n=21)
atg7KO (n=17)
p < 0.0001
b
Horizontal position (pxl)
KO/KO
WT/WT
WT/KO
c
Swimming distance (mm)
Age (dpf)
NS
d
PiT1
mCherry
MAP1LC3b
atg7 WT
atg7 KO
Multiphoton microscopy
e
Pronephros
MAP1LC3b
MAP1LC3b+ structures per pronephros
f
atg7 WT or atg7 KO
(lfabp:1/2 vdbp-mCherry)
mCherry levels by ELISA
Receptors
g
mCherry (pg/ml)
Age (dpf)
h
hATG7:
14 dpf
i
Vehicle
Etomoxir
Swimming distance (mm)
j
mCherry (pg/ml)

Figure 9

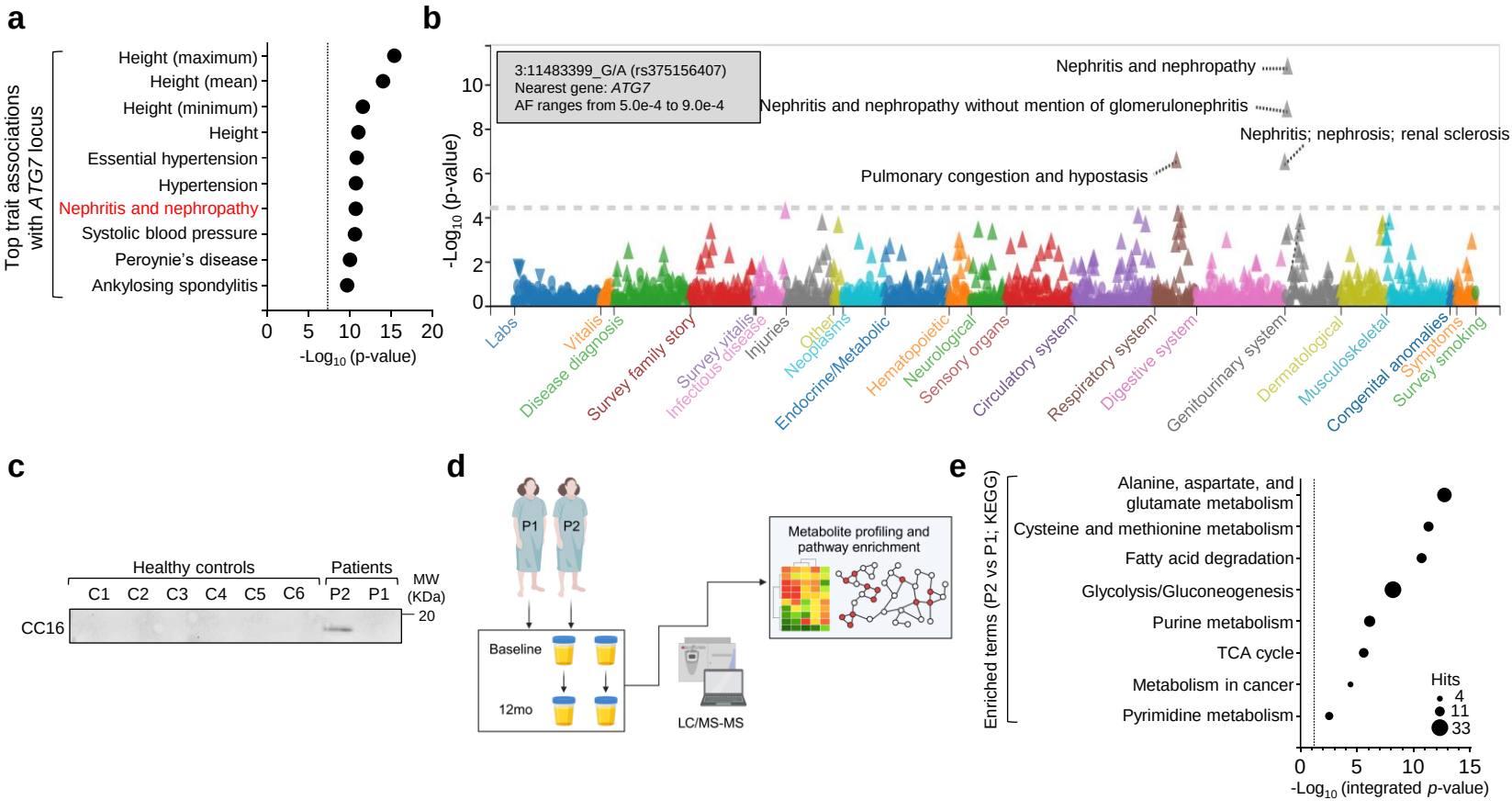
a
Top trait associations with ATG7 locus
Height (maximum)
Height (mean)
Height (minimum)
Height
Essential hypertension
Hypertension
Nephritis and nephropathy
Systolic blood pressure
Peroynie's disease
Ankylosing spondylitis
0 5 10 15 20
-Log10 (p-value)
b
3:11483399_G/A (rs375156407)
Nearest gene: ATG7
AF ranges from 5.0e-4 to 9.0e-4
Nephritis and nephropathy
Nephritis and nephropathy without mention of glomerulonephritis
Nephritis; nephrosis; renal sclerosis
Pulmonary congestion and hypostasis
-Log10 (p-value)
0 2 4 6 8 10
Labs
Vitalis
Disease diagnosis
Survey family story
Survey vitalis
Infectious disease
Injuries
Other
Neoplasms
Endocrine/Metabolic
Hematopoietic
Neurological
Sensory organs
Circulatory system
Respiratory system
Digestive system
Genitourinary system
Dermatological
Musculoskeletal
Congenital anomalies
Symptoms
Survey smoking
c
Healthy controls
Patients
C1 C2 C3 C4 C5 C6 P2 P1
MW (KDa)
CC16
20
d
P1
P2
Baseline
12mo
LC/MS-MS
Metabolite profiling and pathway enrichment
e
Enriched terms (P2 vs P1; KEGG)
Alanine, aspartate, and glutamate metabolism
Cysteine and methionine metabolism
Fatty acid degradation
Glycolysis/Gluconeogenesis
Purine metabolism
TCA cycle
Metabolism in cancer
Pyrimidine metabolism
Hits
4
11
33
0 5 10 15
-Log10 (integrated p-value)

Figure 10

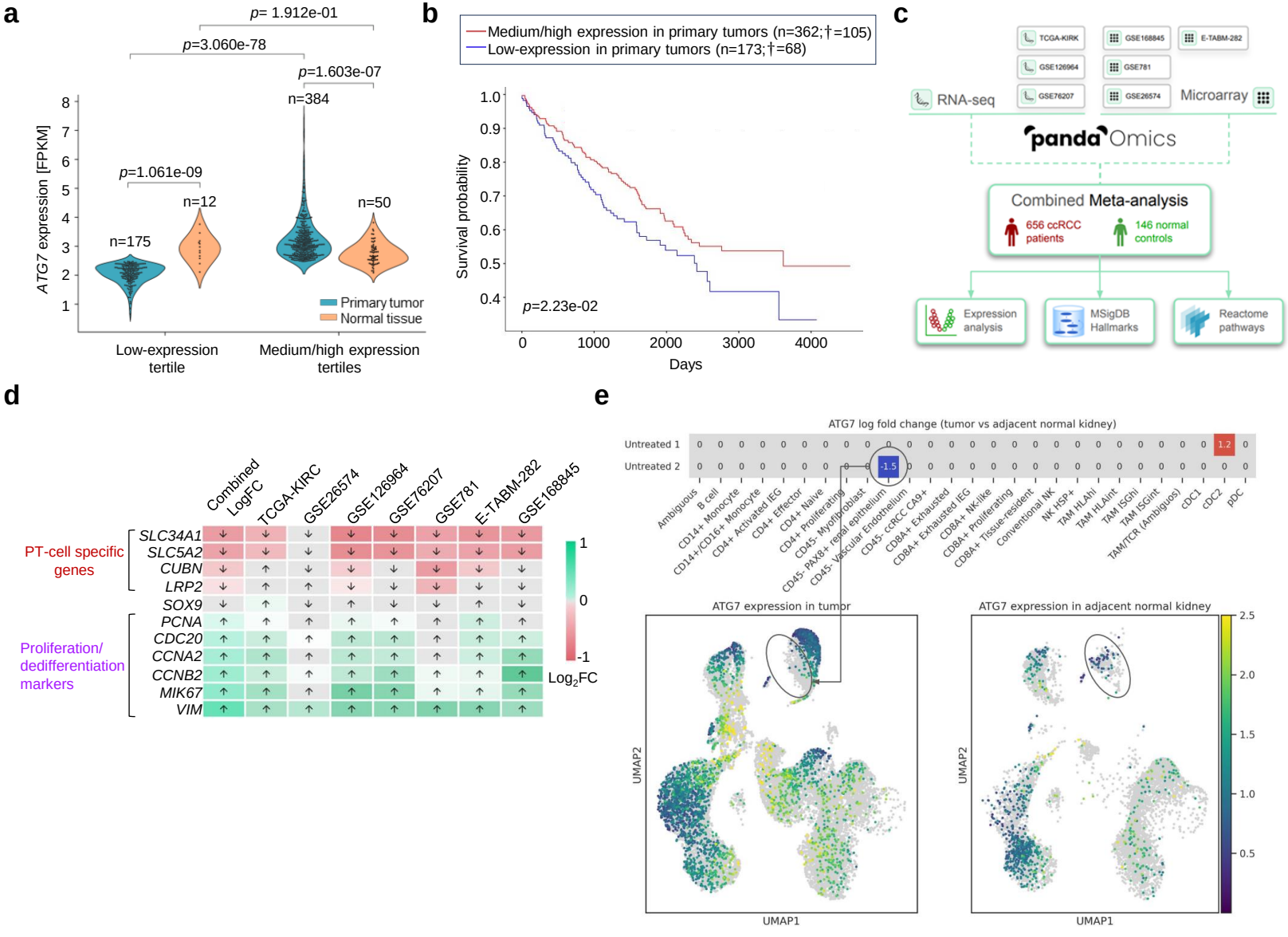
a
p= 1.912e-01
p=3.060e-78
p=1.603e-07
p=1.061e-09
n=175
n=12
n=384
n=50
ATG7 expression [FPKM]
Primary tumor
Normal tissue
Low-expression tertile
Medium/high expression tertiles
b
Medium/high expression in primary tumors (n=362;†=105)
Low-expression in primary tumors (n=173;†=68)
Survival probability
p=2.23e-02
Days
c
TCGA-KIRK
GSE168845
E-TABM-282
GSE126964
GSE781
GSE76207
GSE26574
RNA-seq
Microarray
pandaOmics
Combined Meta-analysis
656 ccRCC patients
146 normal controls
Expression analysis
MSigDB Hallmarks
Reactome pathways
d
Combined LogFC
TCGA-KIRC
GSE26574
GSE126964
GSE76207
GSE781
E-TABM-282
GSE168845
PT-cell specific genes
SLC34A1
SLC5A2
CUBN
LRP2
SOX9
Proliferation/ dedifferentiation markers
PCNA
CDC20
CCNA2
CCNB2
MIK67
VIM
Log2FC
e
ATG7 log fold change (tumor vs adjacent normal kidney)
Untreated 1
Untreated 2
Ambiguous
B cell
CD14+ Monocyte
CD14+/CD16+ Monocyte
CD4+ Activated IEG
CD4+ Effector
CD4+ Naive
CD4+ Proliferating
CD45- Myofibroblast
CD45- PAX8+ renal epithelium
CD45- Vascular Endothelium
CD45- ccRCC CA9+
CD8A+ Exhausted
CD8A+ Exhausted IEG
CD8A+ NK-like
CD8A+ Proliferating
CD8A+ Tissue-resident
Conventional NK
NK HSP+
TAM HLAhi
TAM HLAint
TAM ISGhi
TAM ISGint
TAM/TCR (Ambiguos)
cDC1
cDC2
pDC
ATG7 expression in tumor
ATG7 expression in adjacent normal kidney
UMAP1
UMAP2